Synthesis and Characterization of Ag Doped ZrO_2/ rGO for Photocatalytic Degradation of Methyl Orange

Rana Muhammad Arslan Iqbal

Reg. No. 203343

A thesis that was submitted in partial fulfilment of the degree requirements of

Master of Science in Chemistry

Supervised by: Prof. Habib Nasir

Department of Chemistry

School of Natural Sciences

National University of Sciences and Technology

H-12, Islamabad, Pakistan 2021

FORM TH-4

National University of Sciences & Technology

MS THESIS WORK

We hereby recommend that the dissertation prepared under our supervision by: Rana Muhammad Arslan Iqbal, Regn No. 00000203343 Titled: Synthesis and charcterization of Ag doped ZrO2/rGO for photocatalytic degradation of Methyl Orange Be Accepted in partial fulfillment of the requirements for the award of **MS** degree.

Examination Committee Members

1. Name: DR. AZHAR MAHMOOD Signature: 

2. Name: DR. ASAD MUMTAZ Signature: 

External Examiner: DR. ABDUL MATEEN Signature: 

Supervisor's Name PROF. HABIB NASIR Signature: 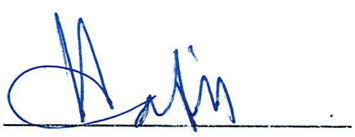


Head of Department

2/9/21
Date

COUNTERSINGED

Date: 03.09.2021


Dean/Principal

Dedicated

To my parents, family and friends

Acknowledgements

At first sight, I am thankful to Almighty Allah, for his uncountable blessings who has given me

The ability to complete my research work. Blessings upon Holy Prophet Hazrat Muhammad (SAW).

Special thanks to all the people who guided me through this period and led me write my thesis.

Primarily, I want to express my appreciativeness to my parents for their love, support, and prayers, without which I would not have been able to accomplish my objectives.

I am grateful to **Prof. Dr. Habib Nasir**, my supervisor, for his help and advice throughout my research. He has the solution to every problem I have faced during my MS.

He explained me everything like a child. He is always available to guide his students. I am thankful to him.

I am also thankful to my **GEC** members **Dr. Azhar Mahmood** and **Dr. M. Asad Mumtaz** for their help and guidance throughout my research.

I am obliged to **Dr. Azhar Mahmood, HoD Chemistry**, for creating a conducive research environment. I would want to express my gratefulness to all of the instructors and staff at **SNS** for their constant support and friendliness. I acknowledge SCME and USPCAS-E for providing me characterization facilities.

Thanks to all my lab fellows, my class fellows and my research fellows. Special thanks to my friends **M. Uzman, Adeel khan, Zia Ur Rehman Goraya, Abid Munir, Abdul Sammad Butt, Muhammad Mobin Ul Haq, Effat Sitara, Tehmina Akhtar and Naima khan** for their help during my research. Without your support my work would not even be possible. Thanks for creating such a friendly environment in lab and university.

Thanks to all my family for their prayers and support without which my work would not even be possible.

Rana Muhammad Arslan Iqbal

Abstract

For all life on Earth, water is one of the most important natural resources. Any chemical, biological, or physical alteration in water quality that harms living organisms or renders water unfit for intended use. The textile industry is one of the largest users of water in the industrial sector. Dyeing and finishing stages in the textile sector are the principal producers of wastewater with complex properties. It interferes with photosynthesis in plants, lowers soil fertility, and hence slows plant growth. It also raises the risk of aquatic life being harmed. It causes a variety of dangerous disorders in humans, particularly carcinogenic ones. Chemical, physical, and biological procedures can all be used to remove dye. Ozone, Fenton reagent, and photocatalytic reactions are some of the chemical approaches used. Adsorption, ion exchange, and filtration/coagulation are examples of physical dye removal procedures, while aerobic degradation, anaerobic degradation, and biosorption are examples of biological dye removal methods. In this study, hybrid nanocomposite of Ag_xZrO_2/rGO was successfully synthesized through facile hydrothermal method. The procedure advents with the synthesis of ZrO_2, then the as synthesized catalyst was critically evaluated by X-ray diffraction (XRD), in order to determine its crystallinity. Scanning electron microscopy (SEM), was utilized for morphological analysis while Energy-dispersive X-ray's spectroscopy (EDX) confirmed its elemental composition. Fourier Transform Infrared Spectroscopy (FTIR), identified different functional entities, UV-vis Diffuse reflectance spectroscopy (UV-Vis-DRS) for band gap determination, and Photoluminescence (PL) for the determination of electrons-holes separation. The $Ag_{0.04}ZrO_2$/rGO (1:1) photocatalyst has a high visible light absorption compared to $Ag_{0.04}ZrO_2$ and ZrO2, permitting efficient photocatalytic degradation of methyl orange MO. The effect of solution pH and catalyst loading on the photodegradation of methyl orange (MO) was also studied. $Ag_{0.04}ZrO_2$/rGO showed

the highest photocatalytic activity for methyl orange degradation due to its absorbance properties. Because of the hybrid nanocomposite's low photo corrosive nature, reusability tests revealed that it has excellent cyclic stability for five repeated cycles. . In contrast to $Ag0.04ZrO_2$ and ZrO_2, the $Ag0.04ZrO_2$/rGO photocatalyst has excellent visible light absorption, allowing for effective methyl orange photocatalytic degradation. $Ag0.04ZrO_2$/rGO produced the highest rate of methyl orange degradation (87%) due to the low rate of electron and hole pair recombination between Ag and ZrO_2 heterojunction. The photo-assisted degradation of MO followed pseudo-first order kinetics, according to the kinetic simulation report. The $Ag0.04ZrO_2$/high rGO's efficiency can be attributed to heterojunction formation, porous structure, and large active surface area.

Contents

List of Figures

Chapter 1

Introduction

Many manufacturers have revolutionized their resources to meet public demands for paints, textiles, leather, plastics, and cosmetics as a result of recent advances, but they have been discovered to be dumping a large number of organic contaminants into the atmosphere, which are not only toxic to plants and animals, but also have a greater resistance to degradation over time. Because the bulk of these are poured into bodies of water, they affect water quality metrics as biological oxygen demand (BOD), chemical oxygen demand (COD), colour, and odor [1, 2]. For instance, a very little amount of colored contamination greatly affects food production under water, resulting in a major loss to the ecological pyramid. So, there is a greater need to remove such contaminations from environment. Relation of industrial development and discharging contaminants also demands technological development in order to respond to such problems by devising methods to overcome this issue [3, 4].

Many techniques like ozonation, incineration, filtration, adsorption and coagulation are normal in practice. These methods have their own limitations and advantages, like filtration cannot be used for soluble impurities while incineration of some leads to the release of some lead to the release of toxic gasses [5]. Adsorption on solid materials and coagulation are effective but far much expensive. Biological decay technique is also in use but it takes longer time to mineralize. However, advanced oxidation processes (AOPs) have been found to be effective to eliminate those effluents from aqueous mediums [6].

Some recent research agrees that AOP based photocatalysts are not only prized candidates but also benefit with complete digestion at ambient conditions. AOPs are successful due to the production of hydroxyl radical (·OH) [7] a potent oxidizing agent, strong enough to remove non-biodegradable substances with ease, so Photocatalytically (figure 1**)** favored AOP emerged as strong candidates for organic waste mineralization, using Semi-conductor as catalyst like TiO_2, ZnO, ZnS,Fe_2O_3 etc [8, 9]. Research is done on TiO_2 and ZnO pertaining to their nature friendly characteristics cost effectiveness, stability and good photoactivity [10-13]. In the 70s, when first prominent work was reposted, a keen interest in scientists was developed in heterogeneous photocatalysis and many advantages were found over conventional techniques like complete mineralization, no harmful by-products, less or no polycyclic compounds and rapid results. With the advent of nanoscale technology, their catalytic activities were much enhanced as properties of material differ at nanoscale as compared to macroscale [4, 14, 15].

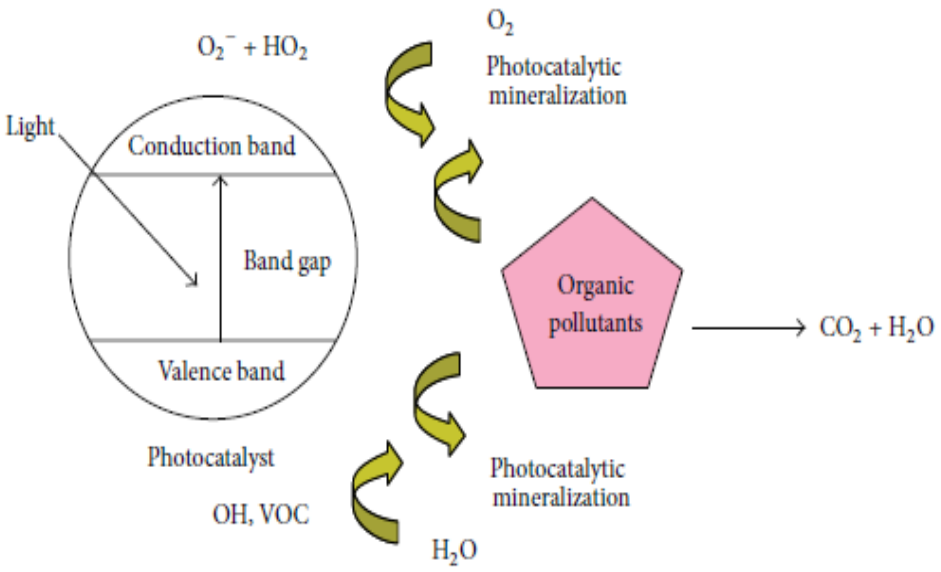

Figure 1: Photocatalytic destruction of organic pollutants.

1.1 Reaction Mechanism

Abasement by a photocatalyst occurs periodically. It involves adsorption, desorption, generation of electron-hole pairs, their recombination and driven chemical reaction. A prevailing mechanism of an organic molecule undergoing photocatalytic degradation is shown. It begins with photons with a minimum energy greater than or equal to the catalyst's band gap energy exciting a photocatalyst (PC). Electrons absorb energy (hν) and transfer it from the valence band to the conduction band, leaving holes (h+) in the process. [16 17]

$$PC + h\nu \longrightarrow e_{CB}^{-} + h_{VB}^{+}$$

Here, hv denotes the photon energy needed to form these electron-hole pairs. The O_2 adsorbed on the surface easily captures the electrons that have been transferred to the conduction band and transforms them into superoxide radicals.

$$e_{CB}^{-} + O_2 \longrightarrow O_2^{\cdot -}$$

By reacting with water, the superoxide radical is involved in the release of hydroxyl and hydroperoxide radicals. To degrade organic contaminants, these radicals are powerful oxidizing agents.

$$O_2^{\cdot -} + H_2O \longrightarrow HO_2^{\cdot} + OH$$

The holes formed by electronic transitions, on the other hand, are able to trap hydroxyl present on the surface, resulting in hydroxyl radical.

$$h_{VB}^{+} + OH^{-} \longrightarrow OH_{ad}$$

$$h_{VB}^{+} + H_2O \longrightarrow {}^{\cdot}OH + H^{+}$$

And in the end, the organic molecule mineralizes to CO_2 and $_{H2O}$

$${}^{\cdot}OH + \text{Organic molecules} + O_2 \longrightarrow \text{Products}(CO_2 \text{ and } H_2O)$$

Recombination of positive holes and electrons could take place and it can hinder the catalytic ability of photocatalyst.

$$E_{CB}^{-} + h_{VB}^{+} \longrightarrow PC$$

1.2 Methods to prepare Nanomaterials

In nanotechnology, two fundamental approaches are used for the synthesis

1. Top-down approach
2. Bottom-up approach

Photocatalysis are synthesized by the following common methods:

- Sol-Gel method.
- Solvothermal synthesis
- Synthesis via co-precipitation
- Synthesis via reverse micro-emulsion

1.2.1 Sol-Gel Method

Figure 2 depicts a schematic diagram of photocatalyst synthesis using Sol-gel technology. Precursors for catalyst synthesis are first dissolved in a chosen solvent, then precipitating agents are added drop by drop while stirring vigorously. It will produce a gelatinous substance that can be removed from the solvent by raising the system's temperature to near or just above the solvent's boiling point. To produce the desired nanocatalyst, the fully dried gel is levigated and sintered. [18, 19].

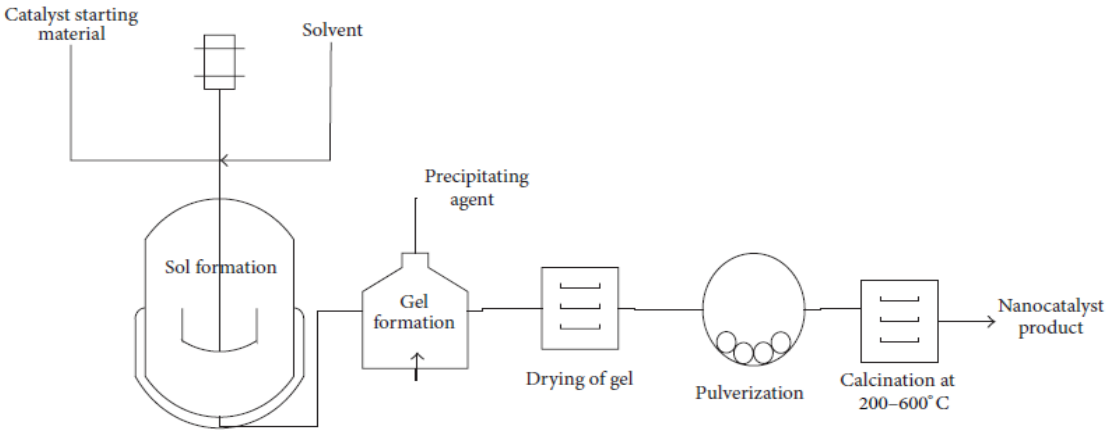

Figure 2: Sol-gel synthesis of photo-catalyst.

1.2.2 Solvothermal Method

In this technique uniformed sized nanomaterials are produced under special conditions but give a good yield of products. First of all, the reacting materials are dissolved in a suitable solvent followed by the addition of a precipitating agent, then this mixture is loaded into Teflon lined autoclave, followed by heating at 100-200 °C for 15-20 hrs depending on pressure. Then, the autoclave is allowed to cool, and the solid particles are carefully cleaned with ethanol and water before being

vacuum dried [20, 21]. Figure 3 depicts a general scheme for developing nanocatalysts using the solvothermal process.

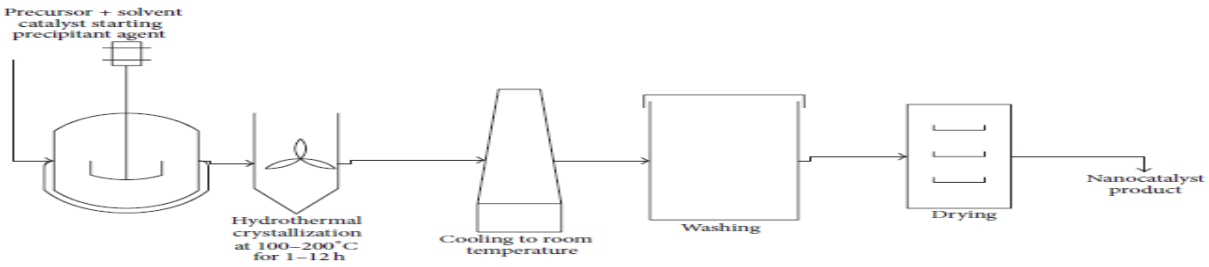

Figure 3: Hydrothermal synthesis of photo-catalyst.

1.2.3 Co-Precipitation Method

As the name indicates, there is a foreign aid provided by a doping agent. Both the required salts and the doping agent are dissolved separately. Then these mixtures are stirred together vigorously to create a homogeneous environment. Sonication can also aid in creating homogeneity. A dropwise addition of NaOH to the precursor solution leads in precipitation after a period of continuous stirring. After that, the precipitates are filtered and washed. The totally dried crystals are calcined at 500 °C for 5 hours to generate the required nanosized particles[22]. The Co-precipitation process is shown schematically in Figure 4.

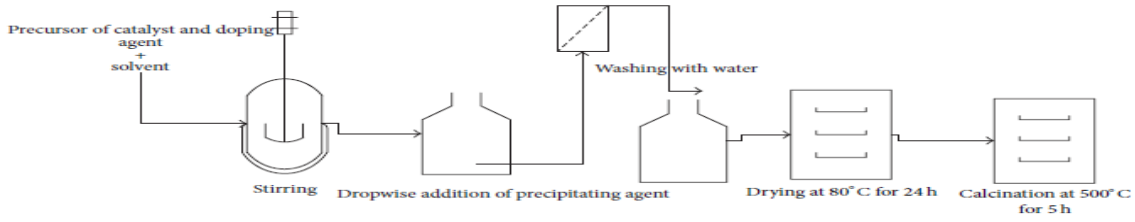

Figure 4: Co-precipitation synthesis of photocatalyst.

1.2.4 Reverse Microemulsion

Figure 5 shows a flowchart of reverse emulsion method. Here surfactants and co surfactants play a crucial role in creating nanoparticles. It involves the creation of 2-3 mixtures separately. Surfactants and co-surfactant are mixed in a suitable solvent. A solution of ammonia is also prepared and stored separately. Precursors' solution is prepared by dissolving it in water. Both the mixtures are mixed separately with surfactant solution, creating transparent emulsion solution. The oil phase emulsion containing precursor salts is termed as mixture A while that containing ammonia as mixture B.

The mixture A and mixture B are then mixed under vigorous stirring until a clear solution is obtained. This mixture is left to age for 2-3 days.

After aging, the nanocatalyst are then separated by centrifugation, washed and calcined to obtain good yield of nano-photocatalyst [23].

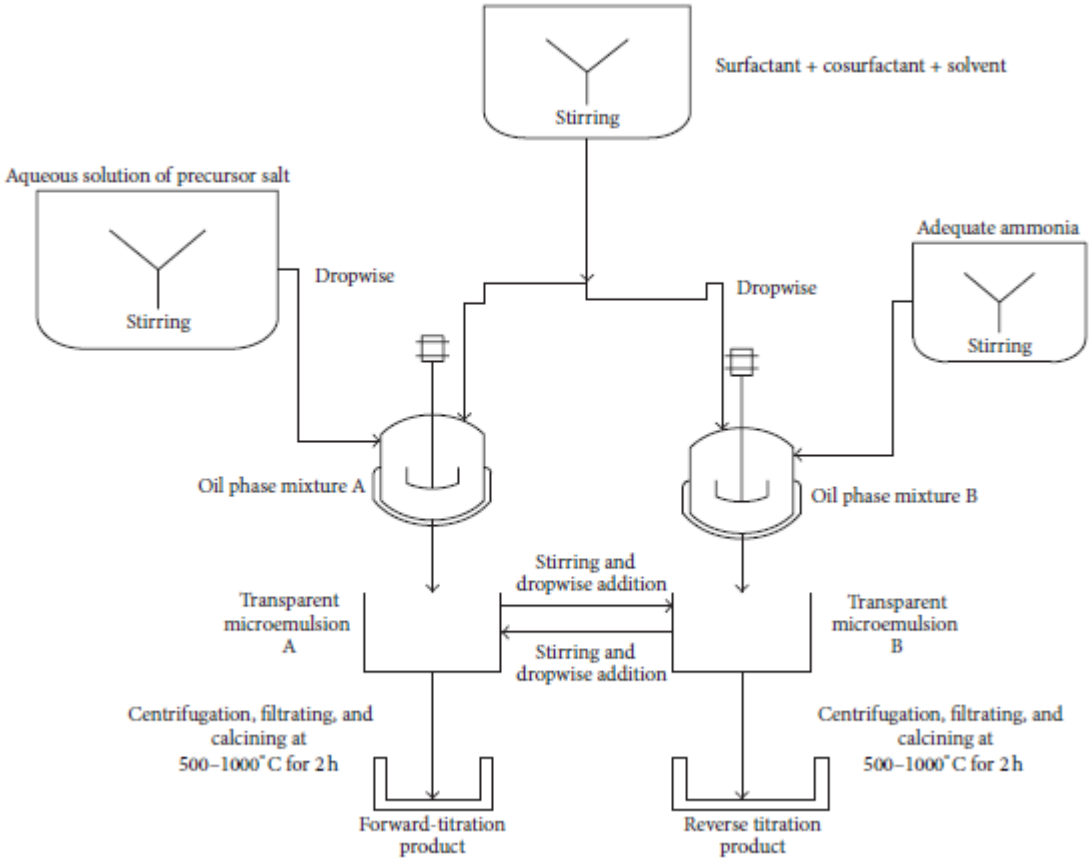

Figure 5: Reverse microemulsion method for synthesis of photocatalyst.

1.3 Parameters affecting Photo-degradation

The catalytic activity of a photocatalyst depends upon many parameters like

- Doping ratio
- Method of preparation
- Light intensity
- Catalyst loading
- Analyte concentration
- pH

- Temperature
- Nature of support
- Nature of analyte

Thus, there are plenty of parameters that are found to be affecting the degradation activity.

1.3.1 Method of Preparation

It is found that a catalyst if prepared by different methods, shows different properties, and a lot of work has been done by scientists to modify the existing routes of synthesis. When comparing the photocatalytic activity of lab created TiO_2 generated hydrothermally to TiO_2 formed at high temperatures, lab synthesized TiO_2 has a higher photocatalytic activity. Because of the loss of water, there are fewer hydroxyl moieties near the surface, resulting in a drop-in activity [24, 25]. In catalytic activity surface area, surface energy and size matter a lot, and was found to be influenced by its mode of preparation. But when size of nanoparticles is reduced it offers greater surface area but their surface energy also increases which can cause agglomeration resulting in lowering of surface area. Thus, losing porosity of the material because of this organic molecule can't reach inter particle spaces and the photocatalytic activity is wiped out [26]. In order to avoid this, a modification of normal sol-gel route was introduced, where steric acid an organic molecule is used as a capsule. These molecules encapsulate nanoparticles so agglomeration is avoided due to repulsion. Other surfactants can also be used as stabilizing agent to prevent recombining of the nanoparticles [27].

1.3.2 Concentration of Decomposing Species

It is also observed that if you over-flood the catalyst surface with organic compound, its catalytic activity is hindered. As they occupy active sites, light causing excitation will not reach catalyst surface

thus no photocatalytic activity [28]. The generation of hydroxyl ions, which are involved in catalytic degradation, is less likely when a large number of organic molecules are adsorbed on a surface. Another observation reveals that if the organic content is overloaded, the transparency of the solution decreases resulting in decrease in penetration of light [29].

1.3.3 Use of Dopants

It is reported that adding a dopant to a photo catalyst improves photocatalytic efficiency by lowering the band gap [22], creating oxygen vacancies, increasing surface area, and allowing for better organic molecule adsorption [30] improved electron trapping [31].

All of these catalytic engineering is in charge of producing more electron hole pairs [32] and make the as synthesized photo catalyst exhibit robust photo catalytic activity under visible light [32-36]. Interstitial and substitutional doping are the two forms of dopant addition in the catalyst. While doping in the metal oxide the radius of the lattice ions is greater than the doped ion, and the lattice space supports better piercing of doped ions. In the latter scenario, however, lattice ions are replaced by dopant ions. Adding dopants to nano catalysts improves their electrical characteristics and their ability to absorb visible light, according to studies. To put it simply, they make the catalyst to exploit the solar spectrum in visible region effectively [2, 37]. It is noteworthy that beyond optimum level of doping concentration has negative effects on photocatalytic activity by decreasing surface area and boost the electron hole pair recombination and as a result of it distance between trap sites reduces rendering the catalyst inefficient or perform poorly [38].

According to Tian et al., increased dopant concentration produces a rise in the composition of rutile, which favors transition from anatase to rutile phase by diminishing anatase's thermal stability. Adding a dopant to mesoporous nanoparticles reduces photocatalytic activity by blocking surface sites. Tong

et al., Doping, on the other hand, enhanced the nano catalyst's surface area by enlarging the mesoporous structure. [39].

1.3.3.1 Noble Metals as Dopants

Introducing noble metals as dopants is also a well-studied phenomenon. However, it is necessary to understand that these metals are effective as dopants due to better adsorption of organic molecules [40, a reduction in electron/hole recombination due to increased electron excitation and electron hole separation [41] and Fermi level equilibration between the photocatalyst and the added dopants. This equilibration is reported to play a vital role in attaining the lower band gaps. This phenomenon has been well studied in ZnO based nanocatalysts where Pt is added to avoid the photo corrosion of the catalyst and it enhances the life time of the catalyst as well [42]. Ag and Au doped TIO_2 catalyst are reported to degrade direct red 23 and acid green 16 dyes up to 97 and 98%. However, both the catalysts were synthesized by photo reduction and impregnation method with optimum doping concentrations of 3 and 0.8 wt%, respectively [43, 44].

1.3.3.2 Non-Noble Metal Doping

Doping with other nonmetals in bi or tri metallic composites plays a crucial role in morphology and particle size tuning [45] and crystal structure as well. Moreover, they are also reported to enhance the specific surface area which is prerequisite for better photocatalytic activity [46].

A study of Ni@ZnS nano catalyst, prepared by coprecipitation method, degraded methylene blue dye up to 50% with an irradiation time of 120 mins having a doping concentration of 0.02 mol% [41]. In another study, 100 % degradation of phenol has been achieved by Nb@ZnO and Co@TIO_2 nano catalysts prepared by friction stir processing (FSP) and combustion techniques with a doping

concentration of 0.50 and 0.1 mol%, under UV irradiation in 18.40 mins and 45 mins, respectively [47, 48].

1.3.3.3 Nonmetallic Dopants

Studies have confirmed that anionic dopants are easy to process and provide greater stability than metal dopants and demonstrate better photocatalytic activity with better quantum yields under UV irradiation [49]. However, Photocatalysts having anion dopants capable of performing in visible light are also reported [50]. The ability of anionic species such as nitrogen, carbon, phosphorus, and fluorine to shape a new impurity energy level close to the valence band that preserves the expanded band gap for maximum performance has been examined [51-52]. The substitutional and interstitial incorporation of nitrogen into photocatalyst structure has been well studied among anionic ligands. Increased ZnO/TiO_2 concentration increases surface area but decreases photocatalytic activity in activated carbon hybridized nano photocatalysts because the activated carbon's pore openings get clogged [52].

1.3.3.4 Earth Metals Doping

Earth metal ions are reported to inhibit the phase transition in the preparation of TiO_2 nano catalyst and the affect remains same with nonmetals and even by combining nonmetals and non-earth dopants [30, 45]. It is the bonding between TiO_2 and rare earth elements that inhibits the phase transition by stabilizing the anatase phase.

Moreover, doping with rare earths profoundly inhibits the size of nanocrystals to grow [53] on the catalyst surface leading to the production of earth metal-O-Ti linkages. *Shi et al*, studies established the above findings as they observed enhanced lattice distortions in in doped nano catalysts as Ti ions gets replaced by the added dopants and overall crystal structure gets distorted due to unnecessary

expansion. As a result of this there is facile adsorption of O_2 molecules as electron traps benefiting from lattice distortion and expansion. This leads to decreased electron hole pair recombination's and better photocatalytic activity is observed [54]

1.3.4 Catalyst Loading

Since it is generally known that increased active sites or surface area are dependent on photocatalyst dose. As a result, organic pollutant photocatalytic degradation is improved. Because of the higher levels of hydroxyl radicals created during irradiation. [55]. Considering the amounts of catalyst loaded, it is noted that at lower concentrations degradation is also low. However, if loading goes beyond the optimum value degradation may be lowered due to greater suspension and scattering of light leading diminished infiltration depth of photons [56]. Supporting this study, it is studied that agglomeration of nanoparticles decreases the activity of the catalyst due to the less exposed and formed number of surface-active sites. Along sides, activated molecules get deactivated as they collide with other activated molecules and it does decrease the activity [57].

1.3.5 Calcination Temperature

Tuning the calcination temperature of the as synthesized photocatalyst help optimize and inculcate good to excellent optical property, crystal size, and crystal structure [58]. In commonly encountered syntheses of nano catalysts higher calcination temperatures are reported to support particle growth and render the catalyst less efficient by decreasing the surface area [57]. Anatase phase in TiO_2 has a higher thermal stability than rutile phase due to its better adsorptive capability for organic molecules, resulting in higher anatase phase concentration at higher temperatures and more catalytic activity than rutile phase. However, in doing this anatase gets befitted from low electron hole pair recombination's

[59]. Similarly, Sun et al. predicted that as temperature rises, doping nitrogen with TiO_2 will become more complicated and messier due to larger crystal particle sizes. [60].

1.3.6 Calcination pH

The calcination pH of the aqueous dye solution, as well as the superficial charge and oxidation potential of the valence bond in respect to the constructed photocatalyst and the superficial charge of the photocatalyst, influence catalytic activity in terms of dye adsorption and dissociation [61]. When the pH of a nano catalyst is raised above its isoelectric point, the surface becomes negatively charged, and when the pH is reduced, the exterior becomes positively charged. Higher pH values of the aqueous solution help in the adsorption of the cationic molecules and in smaller pH conditions more anionic molecules will be adsorbed [55]. Yet, it has been observed that at higher pH levels, more hydroxyl radicals are produced, which aid in the degradation of organic molecules; however, the degradation rate is slowed and less adsorption occurs on the catalyst surface if the concentration of H^+ ions exceeds a particular threshold. However, in lower pH or more acidic conditions abundant positive charge lessens the adsorption of cationic species and overall activity of the catalyst decreases. So, conclusively, an optimum pH for different organic solutions provides better degradation efficiencies [62]. Prado and Costa [63] have discovered that malachite green degradation is substantially higher in acidic than in basic conditions.

1.3.7 Impact of Oxidants

The recombination of electron-hole in photocatalysts can be reduced by accumulation of electron accepting species to the matrix, such as $(NH_4)_2S_2O_8$, H_2O_2, $K_2S_20_8$, and $KBrO_3$ [43]. To increase

photocatalytic activity, H_2O_2 is widely employed. The following mechanism shows how H_2O_2 affects photocatalytic degradation:

$$H_2O_2 + O_2^{\cdot -} \longrightarrow {}^{\cdot}OH + OH^- + O_2$$

$$H_2O_2 + hv \longrightarrow 2{}^{\cdot}OH$$

$$H_2O_2 + e_{CB}^- \longrightarrow {}^{\cdot}OH^{+}{}^{\cdot}OH^-$$

The rapid degradation of organic species occurs when the concentration of H_2O_2 is increased. Photolysis of H_2O_2 produces the OH radical, which grabs electrons and prevents electron-hole pairs from reuniting, increasing the likelihood of the OH radical and O_2 developing on the surface. However, beyond a certain concentration of H_2O_2, increasing the concentration of H_2O_2 reduces the rate of degradation due to the formation of peroxide radicals, which act as a hole [64].

1.3.8 Role of Light Intensity

Light intensity plays a vital role when a semiconductor photocatalyst absorbs energy, it creates holes in the valence band and electrons in the conduction band. Due to absorption of this energy electrons to go from the valence band to the conduction band. The rate of photocatalytic degradation rose as the intensity of incoming radiation rose, showing that increasing the intensity of incoming light can boost the likelihood of catalyst excitation [65]. In photocatalysis, however, the reunion of electron-hole pairs is difficult. When the light intensity is low, the spacing of electron-hole pairs is reduced, resulting in less free radical generation and organic molecule breakdown. Only high-intensity light can be used to prevent this and good photocatalytic activity [66].

1.3.9 Consequence of Temperature

As the temperature rises, the photocatalytic performance of the catalyst for the destruction of organic contaminates enhances. As the photocatalytic degradation of the organic species is directly related to temperature. When the temperature of organically contaminated solution is raised, bubbles occur in that solution, following in the formation of free radicals. Furthermore, by blocking electron-hole reunion, the increase in temperature helps the overall degradation reaction [67].

1.3.10 Consequence of the Support

The use of a support for the nanophotocatalyst inhibits agglomeration and sintering by keeping the nanoparticles distributed [61]. Charge separation (high electric conductivity supports) and organic molecule adsorption are two ways supports can boost photocatalytic performance. In order to ensure reusability, most nano catalysts are immobilized with a support/magnetic coating [68] and also aids in Organic molecule adsorption to improve photocatalytic degradation performance. The emergence of hydroxyl radical on the support surface has the potential to degrade organic contaminants adsorbed on mesoporous (support) materials. [69].

1.3.11 Zirconia (ZrO_2)

Zirconia has recently received a lot of attention as a catalyst support, partly because it's more chemically inert than traditional supports like silica or alumina, and partly because it's been shown to have unique interactions with the active phase, leading to differences in the activities and selectivity of the resulting catalysts. A variety of phase structures can be used to make zirconia. Gel precipitation produces the unstable tetragonal phase; however, the material becomes unstable when calcined at higher temperatures, with the area falling by as much as 97 percent at 850 °C. Sintering is caused by a

surface transport process, which results in a phase transition to the monoclinic form, which is the most stable at normal working temperatures. Zirconia is a nontoxic, chemically inert transition metal oxide having superior thermal stability owing to its high crystalline forms such as monoclinic, tetragonal and cubic [70] The wide band gap of zirconia nanoparticles (3.3 eV to 5.1 eV) can be used in sensors [71-72] fuel cells,[73] and catalyst in various chemical reactions, and dielectric materials. [74-77]

1.3.12 Graphene

Graphene, a single atomic layer, two-dimensional graphitic carbon material, is suitable for use as a photocatalyst support material due to its unique properties, such as excellent electrical conductivity, high chemical stability, large specific surface area, and unique electronic and mechanical properties. [78,79]. Graphene is being considered for a range of applications, including photovoltaic catalysis, supercapacitors, energy storage nanoelectronics, and lithium-ion batteries, due to its exceptional characteristics [80, 81]. Graphene has been discovered to increase the charge separation rate of titanium dioxide in a few recent studies [82]. According to Shen et al., TiO_2/RGO composites produced using an ionic liquid-assisted one-step hydrothermal procedure have good photocatalytic activity. For the destruction of RhB in aqueous solution, Sher Shah and his colleagues employed TiO_2–RGO nanocomposites with increased photocatalytic activity [83]. The photocatalytic behavior of graphene encased shallow TiO_2 nanospheres as a photocatalyst was examined by Zhang and his colleagues [84]. To degrade MB solution, Yan et al. used RGO/TiO_2 composites as photocatalysts. [81.] The generated materials show excellent photocatalytic properties due to the good link between TiO_2 and GO. Nanoparticles with unique structures and excellent properties have attracted a lot of attention as nanotechnology has grown rapidly. Due to their peculiar physical and chemical properties, hollow nano spheres have aroused a lot of attention, and they've been widely used in a variety of

industries, including photocatalysis, sensors, energy storage, drug delivery, and Lithium-ion batteries [85-87].

1.4 Characterization Techniques

Characterization techniques are used to analyze the material. The methods tell both about the physical and the chemical properties. These include spectroscopic analysis. I have used various techniques which are given in figure 6.

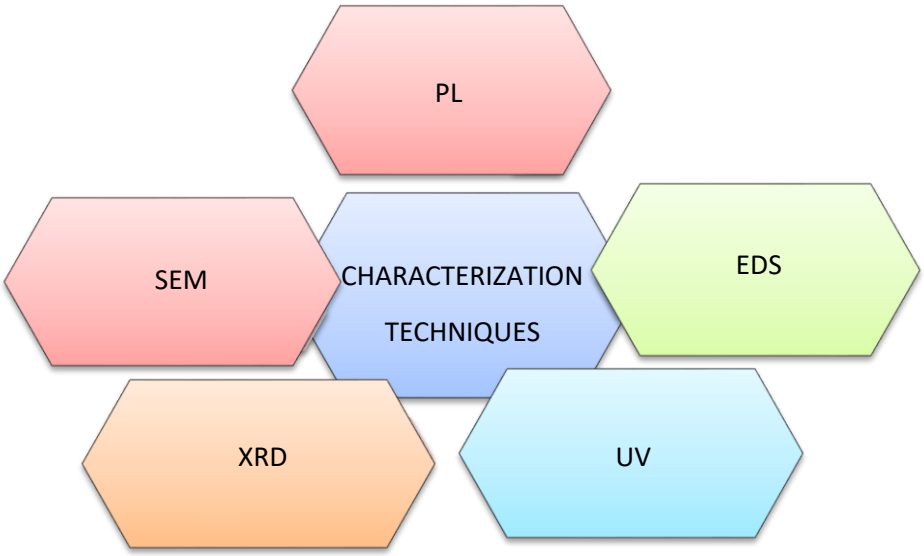

Figure 6: Analytical techniques used for Characterization.

1.4.1 UV-DRS Spectroscopy

UV-DRS spectroscopy is a form of spectroscopy in which molecules absorb light in the UV range between 200 and 400 nanometers. Electrons are stimulated from the ground state to the excited state as a result of this absorption. As a result, the amount of UV radiation absorbed is equal to the energy difference between the ground and excited states. UV-Vis spectroscopy has a wavelength range of 200-800 nm. Transitions from the occupied highest molecular orbital to the unoccupied lowest molecular orbital are the most popular. The lowest energy occupied molecular orbital that corresponds to bonds is the s orbital. Nonbonding orbitals are the p orbitals. The highest energy occupied orbitals are $\pi^*$and σ^*. Some important transitions that correspond to highest energy are given below also shown in Figure 7 [20].

- n to π^*,

- n to σ^*,
- π to π^*,
- σ to π^*
- σ to σ^*

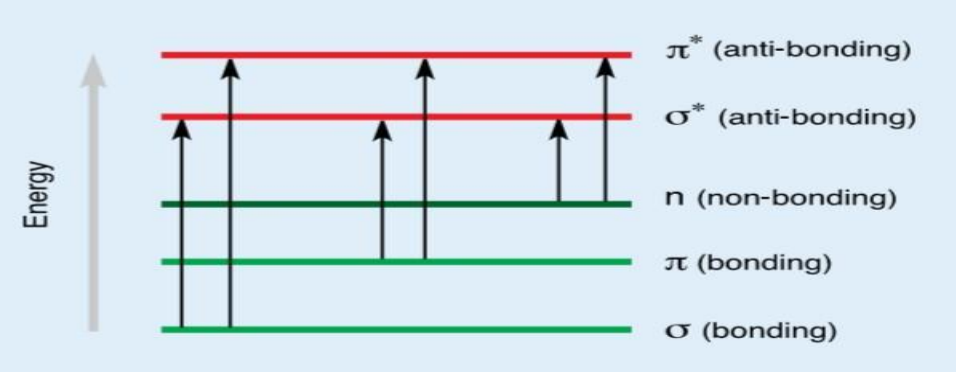

Figure 7: Electronic transition when photon falls on a medium.

Principle

According to Beer-Lambert law, the amount of light absorbed by a material dissolved in a fully transparent solvent is directly proportional to the substance's concentration and the length of the light path through the solution.

$A = \log (I_0/I)$ $A = \varepsilon.c.l$

Thus, from this it is clear that as we increase the number of absorbing molecules the absorption of light is increased. Figure 8 shows the instrumentation of UV-VIS spectroscopy [21]**.**

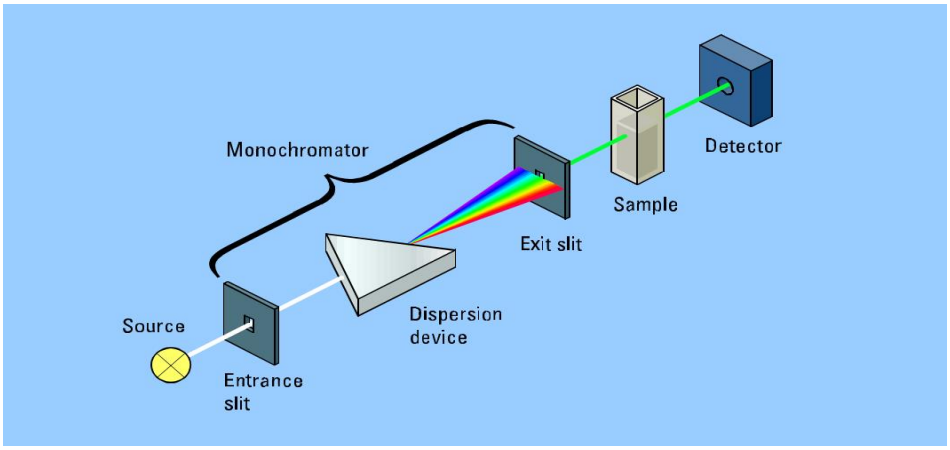

Figure 8: Instrumentation of UV-VIS Spectroscopy

1.4.2 Scanning Electron Microscopy (SEM)

The structural morphology of a substance is typically determined via SEM [15]. In 1931, Max Knoll and Ernst Ruska in Berlin, Germany, devised the electron microscope. The scanning electron microscope (SEM) generates multiple signals on the surface of materials using a high-energy electron beam. These signals reveal the morphology and chemical composition of the sample.

Principle

An electron ray is formed by a source, which is typically a tungsten filament. This ray of electrons is accelerated with high voltage and then passes through lenses to produce a thin electron beam. As the beam scans the material's surface, electrons are expelled and detected by a detector. Figure 9 explains the instrumentation of SEM [22].

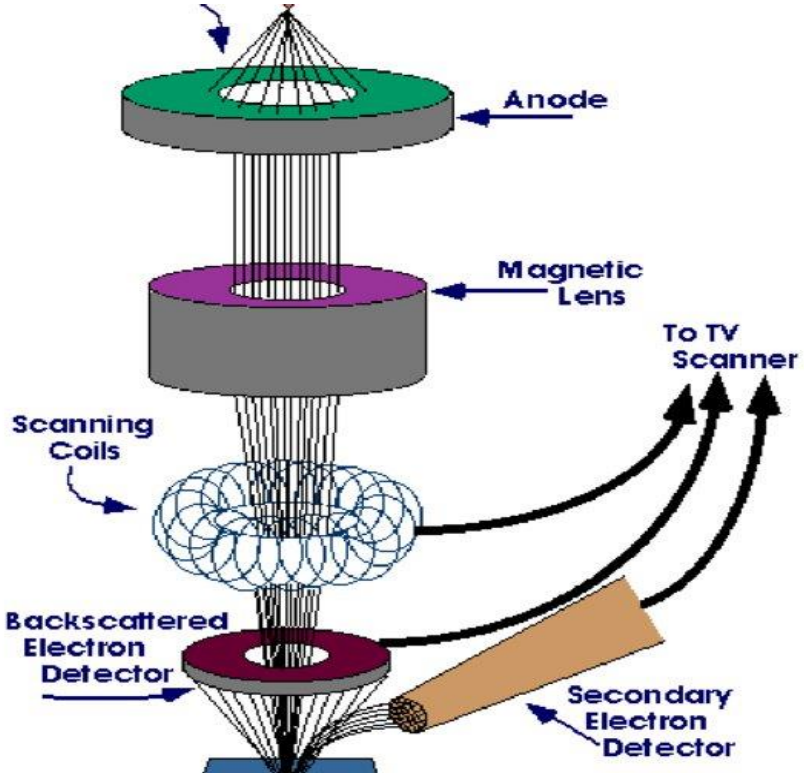

Figure 9: Schematics of FE-SEM.

1.4.3 X-ray Diffraction

This technique gives information about different crystalline phases, their quantitation and matrices of unit cell. In electromagnetic spectrum X-rays cover 0.01 to 10 nm. It is basically used for the identification of phase of a crystalline material. The material that is analyzed is ground and then bulk composition is determined.

Principle

The X-rays are firstly produced through a cathode ray tube. Then they are filtered, collimated and then directed towards the sample. When the condition meets Bragg's law, the sample creates constructive interference.

$$n\lambda = 2d \sin\theta$$

The diffracted X-rays are then detected, treated, and measured. Both diffraction directions should be obtained when imaging the sample at a range of 2θ.

Figure 10 explains the instrumentation of XRD [23].

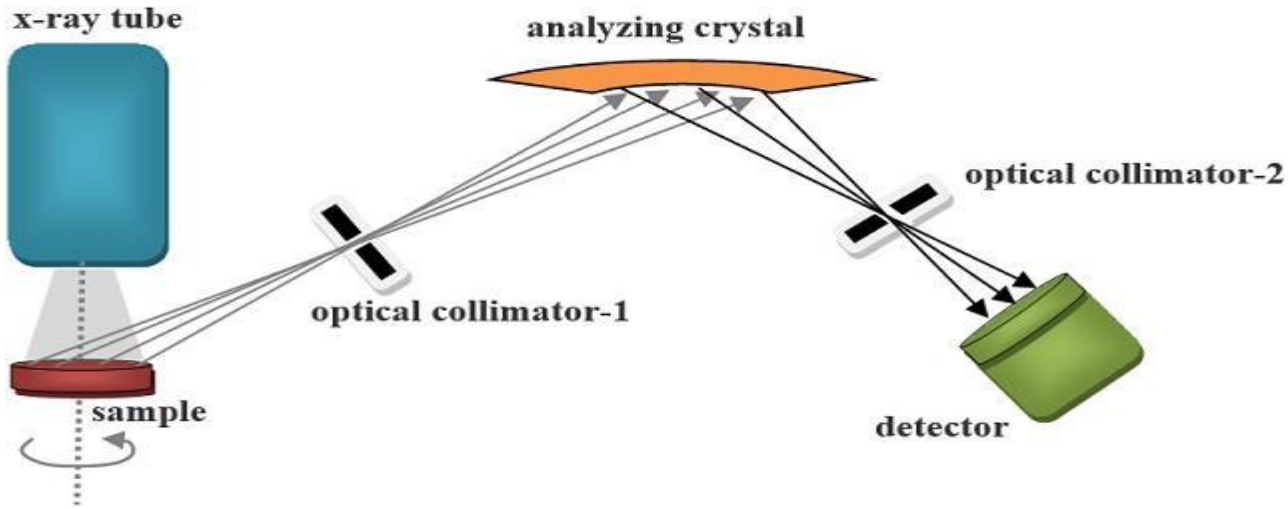

Figure 10: Schematic illustration of working XRD.

1.4.4 Photoluminescence (PL)

Photoluminescence (PL) is a non-destructive optical technique that can be used to locate, investigate, and detect point defects as well as measure material band gaps. Photoluminescence is caused by irradiating the crystal to be described with photons with an energy larger than the band-gap energy of that molecule. In a crystal scintillator, incident photons generate an electron-hole pair. As these electrons and holes recombine, some of the recombination energy will be turned into non-radiative emission and some will be transformed into radiative emission. Photoluminescence is the process of energizing atomic electrons by impinging relatively high frequency (hv> Eg) light onto a substance. Following relaxation, photons will be produced that are unique to the crystal or defect site that produces the light. The detected light signals could be caused by band-to-band recombination, inherent

crystallographic defects (development defects), dopant impurities (added during growth or ion implantation), or other external fault levels An impurity energy level can emit distinct photons from various different types of radiative recombination processes when bombarded with photons with energies greater than the bandgap of the material, allowing the PL spectra to be used to identify the type of semiconductor defect.

This interaction allows for a highly sensitive, qualitative evaluation of native and extrinsic impurity levels inside the content bandgap. In a nutshell, there are three steps to the photoluminescence process [24].

1) Excitation:

Electrons can be driven to higher energy levels by absorbing energy from external sources such as lasers, arc-discharge lamps, and tungsten-halogen bulbs. Electron-hole pairs are formed during this process.

2) Thermalization:

As they relax, excited pairings settle into quasi-thermal equilibrium dispersals.

3) Recombination:

The energy may be released in the form of a lower-energy photon when the electron returns to its original ground state. This process will be radiative or non-radiative in nature. [88].

Chapter 2

Literature Review

2.1 Mixed oxides photo reactivity surface aspects and photophysical properties in aqueous phase for 4-nitrophenol oxidation

Sol gel technique was utilized to create oxides of ZrO_2 and SiO_2 using commercial silica gel and zirconyl chloride. The degradation of 4-nitrophenol in aqueous suspensions of powdered photocatalyst, as well as several surface properties of the powders and photo reactivity performance, are all examined. The photoactivity of the ZrO_2-SiO_2 samples is much reduced when compared to a TiO_2 sample evaluated under the same experimental circumstances. ZrO_2-SiO_2 suspensions had unfavorable optical features than that of with those of TiO_2.

ZrO_2-SiO_2 sample had less significant oxygen adsorption due to the lower degree of hydroxylation with respect to that of TiO_2 [89].

2.2 Degradation of Acetone in Air by using $Ti1\text{-}xZrxO_2$

The procedure of citric acid complexing can be utilized to create stable $Ti_{1-X}ZrxO_2$ anatase solutions. As the zirconium substitution in the lattice increases, the functioning of TiO_2 improves until nominal X = 0.075. According to the characterization data, the increase in activity is attributable to changes in the lattice characteristics and cell length. According to a suggested mechanism, the enhanced activity is induced by lattice O_2^- and O^- species iono sorbed on the surface. [90].

2.3 Doping of zirconia on microstructures

The microstructure, liquid permeability, thermal, and chemical stability of mesoporous composite titania/zirconia membranes were examined up to 25 mol percent zirconia doping. Zirconia has been found to inhibit the phase transition of anatase until it reaches 700 degrees Celsius. By adding up to 20 mol percent, pore size was reduced to 3.6 nm, and nitrogen sorption studies validated the increase in porosity, BET surface area, and pore connectivity. At room temperature and in the pH range, undoped titania and composite titania/zirconia materials were found to be chemically stable from 1–13. The addition of zirconia to titania membranes increased their mechanical strength dramatically. The amount of zirconia doping or the makeup of the permeating liquid had no effect on the permeability [91].

2.4 Study of iron doped zirconium oxides

Iron and zirconium hydroxides were co-precipitated by hydrolysis of an aqueous (Fex-Zr). Analysis of dried samples' thermal decomposition. Different iron species interacted with zirconia in different ways due to the varying preparations.

Zr^{3+}defects were not formed in the solid due to a bulk dispersion of the co-precipitated material. At low calcination temperatures (up to 600°C), the production of surface Zr^{3+} ions were seen in Fex/ZrO_2.In the case of Fex/$ZrO(OH)_2$, such interactions were not seen since X-ray identified a modest dispersion of iron species. Using Temperature Programmed Reduction, we discovered that reducing small Fe_2O_3 particles [92].

2.5 Methyl Red photocatalytic degradation using Ag^{+} doped TiO_2

In this study they used titania and silver doped titania for the catalytic degradation of mixture of two dyes crystal violet and methyl red. The photocatalytic degradation of these were measured by UV visible spectroscopy at their respective lambda max values. To quantify the dye degradation the aliquot was taken at regular time intervals. After 90 minutes of irradiation the dyes were degrade up to 86 %. [93].

2.6 Composites of mesoporous TiO_2–ZrO_2

A single-phase approach was successfully used to produce a series of multi-model mesoporous TiO_2-ZrO_4 composites. ZrO_2 added to multi-modal mesoporous Tio_2-Zro_2 materials inhibited crystalline development and accretion while also inducing restricted phase transitions from amorphous to anatase and anatase to rutile. In this study they looked at the effect of different calcination temperatures and other parameters on TiO_2-ZrO_2 composites. When compared to pure TiO_2, multi modal mesoporous TiO_2-ZrO_2 composites demonstrated increased hydrophilicity and photocatalytic activity in the absence of light irradiation. Photo catalysis, self-cleaning, and other related applications could benefit from this combination [94].

2.7 Monocrystalline cubic ZrO_2 Nanoparticles

Gradual hydrolysis and thermal hydrolysis of solutions of NaOH at 180 ºC primed crystalline ZrO_2 nanoparticles from zirconium iso peroxide. Nanoparticles of mono clinic ZrO_2 with plate like morphology was prepared by mild basic solutions and strong basic solutions result in the formation of nanoparticles of high temperature polymorph with diameter of nearly 5nm. Formation of both above

structures was confirmed by microscopy. Reaction conditions has choice to decide crystallinity and morphology of resulting ZrO_2 nanoparticles. Cubic ZrO_2 has high surface area and show phot luminescent in UV region. ZrO_2 nanoparticles has use in luminescent labels, light emitting substances in nano scale and optical memory systems [95].

2.8 Conversion of Azobenzene to amines by using $Na_4W_{10}O_{32}/ZrO_2$ nanocomposite

In this study they used 2-Propanol as a hydrogen donor, the nano composite was employed at ambient temperature, as a green and recyclable heterogeneous photocatalyst for the rapid and systematic reduction cleavage of azobenzene into their corresponding amines. The reduction cleavage of reducible moieties such as halogen, and -OH occurred without hydrogenolysis or hydrogenation. The photo catalyst was rehashed several times with limited loss of operation and selectivity. The $Na_4W_{10}O_{32}/ZrO_2$ nanocomposite was more efficient at reducing azobenzene, showing that the nanocomposite technique could be a great strategy to boost POMs. In their laboratory, they are testing the photolytic applications and comprehensive mechanisms of $Na_4W_{10}O_{32}/ZrO_2$ and related composites to reduce other substances [96].

2.9 ZrO_2-TiO_2 Mixed Oxides for degradation studies

The tetragonal ZrO_2 proved to be catalytically active for the dilapidation of anionic pigments and was made by solution combustion technique. The alizarin cyanine green (ACG), remazol brilliant blue R, and orange G were photo catalytically tarnished using the aforesaid material. The influence of pH, inorganic, and H_2O_2 on catalytic activity was examined, and the catalyst, like the inorganic salts, demonstrated well-maintained activity over a wide pH range. After learning about ZrO_2's

photocatalytic activity, experiments for mixed oxide catalysts of TiO_2-ZrO_2 for photocatalytic dilapidation of ACG were conducted, with the findings revealing that TiO_2 and 50 percent ZrO_2-TiO_2 mixed oxides behave quite similarly. The dilapidation rates of ACG were dramatically underestimated in the presence of H_2O_2 at concentrations ranging from 3-150mM. High activity without inhibitory effects from inorganic salts, as well as a broad pH spectrum, proved to be particularly desirable for industrial applications [97].

2.10 Mesoporous ZrO_2 for catalytic oxidation of alkenes

In this study they have synthesize zirconia-based mesoporous nanocomposites of heteropoly acid were made using a simple sol-gel process. Non-ionic polymer surfactant helped in the strong and complex networking between anions of PMA and zirconia besides catalyzation. The new nanocomposite obtained showed the mesoporous morphology with 4-6 nm as the pore size. During the oxidation of alkenes, the as-manufactured substances revealed increased catalytic stability and patronizing catalytic ventures. ZrO_2 with 40% PMA revealed wonderful catalytic performance, finer stability enduring permanence during alkene oxidation reactions when compared to PMA free zirconia and other analog catalyst [98].

2.11 Synthesis of Cubic and Monoclinic Zirconia from Zircon

Through the technique of ball mill-aided precipitation, Zircon sand was used to produce destabilized monoclinic and sodium-stabilized cubic phases with Zirconia (ZrO_2) nanoparticles. The effects of processed parameters on particle size, crystalline phase, PSD, aggregation, and morphology are discussed in this paper. According to XRD and EDS study, synthesis at pH 13 yields sodium-stabilized cubic zirconia, while pH 7 yields non-stable monoclinic zirconia. The size of the product's

particles and the crystalline phase are controlled by the precipitation's pH value. Temperature increase of calcination originates the crystal growth that results in greater particle magnitude. Ball milling process was beneficial in a way that it's more flexible and easier to conduct and scale up to commercial production rates. The residual sodium in the material is currently one of the biggest roadblocks in this operation [99].

2.12 Various Mixed oxides photocatalytic action

A sol–gel process is used to make ZrO_2, SnO_2, and CeO_2 nanoparticles, which are then calcined at 550°C. The XRD results indicated that these particles have a tetragonal and monoclinic atom configuration. The photocatalyst combination increased the catalyst's effectiveness as well as the rate of 2-nitrophenol photodegradation. Catalyst reactivity was influenced by the pH of the samples and the makeup of the combination. As a result, mixed oxides of ZrO_2/SnO_2 in pH 4 exhibited the best behavior. Nanoparticles comprising ZrO_2/SnO_2 (as a catalyst) outperform nanocomposite $Zr_{0.8}SnO.2O_2$ in terms of output [100].

2.13 Photodegradation on ZrO_2

When phenol is exposed to 365nm light, it degrades on the outward of ZrO_2. The rate of deprivation slows as the pH rises, but it accelerates linearly as the phenol concentration and light intensity rise. Photonic efficiency of degradation using light of wavelength 254nm is higher than that 365nm. Certain Metal oxides particles boost photodegradation on ZrO_2. Only by suspending semiconductor particles in suspension and passing electrons from the conduction band of phenol-adsorbed ZrO_2 to the semiconductor's conductance band could photoreaction be improved. The size of suspension particles can be assessed using the light scattering technique, which reveals particle aggregation. UV-

C light accelerates the decomposition of ZrO_2, whereas UV-A light promotes phenol degradation. The degradation of phenol and photon flux is shown by first-order kinetics, which decreases as the pH value rises. Degradation with UV-A light is suitably performed through the mechanism of Phenol-sensitized excitation of ZrO_2 [101].

2.14 Properties of ZrO_2 in terms of structure, optics, and photocatalysis

ZrO_2 nanocrystals were made using the microwave combustion technique (MCM). Urea was employed as the fuel during the microwave combustion of ZrO_2 nanocrystals, with no template, catalyst, or surfactant. It was also made using the classic combustion method for comparison (CCM). MCM is a faster method than CCM, according to the results of the comparison. Furthermore, by evenly distributing heat across the bulk of the reaction mixture, MCM forms a nano spherical structure with a narrow particle size distribution. Both CCM and MCM aided in the inclusion of crystal defects by causing ZrO_2 to crystallize quickly. MCM, on the other hand, may be a quick and easy way to make ZrO_2 nanocrystals that improve photocatalytic degradation of 4-CP. For the photocatalytic degradation of 4-CP, ZrO_2– TiO_2 mixed oxide catalysts were examined, and the behavior of ZrO_2– TiO_2 mixed oxides was comparable to that of pure TiO2 [102].

2.15 rGO/ZrO_2 nanocomposite for fluoride removal in water

A simple hydrothermal method was used that included GO and $ZrOCl_2.8H_2O$ to prepare a nanocomposite of rGO/ZrO_2 and this method has been successful in removing the fluoride from an aqueous solution by the process of adsorption. There are a number of factors that actually play an active role in the removal of fluoride from an aqueous solution and these factors include.

1. rGO/ZrO_2 dose,

2. The initial concentration of fluoride,
3. Temperature and pH,

These factors influenced fluoride removal, and it was discovered that the nanocomposite's maximum uptake potential. The surface area of rGO/ZrO_2 is substantial, and at neutral pH and room temperature, maximum adsorption occurs. This is due to two key factors: monolayer fluoride adsorption and the unpredictable and highly endothermic pseudo second order kinetic model. Both of these findings are extremely helpful to water fluoridation. The removal of fluoride from water using this endothermic method was estimated to take 50 minutes. Therefore, the entire process makes it clear that it is actually due to the adsorption process. However, the intraparticle diffusion model and the Reichenberg model suggest that intraparticle diffusion is not the only reason causing this process, it is actually because of the adsorption of fluoride by the rGO/ZrO_2 and its monolayer nature. The DGO values were important because their negative values indicated spontaneity, while their positive values indicated that the entire process was endothermic. The rGO/ZrO_2 is an effective fluoride removal system that works in a variety of conditions, including low temperature, normal pressure, and pH. These findings could be useful in the development of continuous column studies employing rGO/ZrO_2 as an adsorbent for the treatment of fluoride-contaminated water [107].

2.16 SnO_2-ZrO_2 nanocomposite grafted with phosphate

Another study created a nanocomposite of SnO_2-ZrO_2 with phosphate grafting for catalytic synthesis of trisubstituted indoles using in-situ solution processing. Limiting the composition range of SnO_2 and ZrO_2 resulted in a solid solution with the crystal lattice of individual solutions preserved. Both t-SnO_2 and cassiterite-ZrO_2 solutions have Zr and Sn doping, resulting in improved solid solution stability in both cases. By adding positive ions to the surface of SnO_2-ZrO_2 nanocomposites, phosphate grafting and doping increases the surface acidity. The SnO_2-ZrO_2 material was used as a catalyst to produce

structurally different indole derivatives under moderate conditions. The heterogeneous catalytic protocol developed in this study has several advantages, including ease of experimentation, the avoidance of toxic solvents, and the use of fewer reagents [109].

2.17 Comparison of ZrO_2 and TiO_2 for degradation of plastics

Because of its low degradability, plastic accumulation in the environment is a big issue. Reuse, recycling, and the use of biodegradable plastics are all options for dealing with this problem. However, there is yet to be a comprehensive solution to this issue. This research looked at the photocatalytic breakdown of polyethylene and polypropylene. In comparison to TiO2 nanoparticles, the photocatalytic degradation impact of ZrO2 nanoparticles was investigated. TiO2 nanoparticles were made using sol gel, while ZrO2 nanoparticles were made using sono chemistry. This research was able to successfully synthesize TiO_2 and ZrO_2 nanoparticles. Tetragonal TiO_2 nanoparticles in the anatase phase were found. Particles of ZrO_2 are what we're talking about. Using nanoparticle suspensions in a THF medium, these particles were applied to polyethylene and polypropylene. The degradation of the plastics was investigated using FTIR and SEM to look at chemical and morphological changes. In the laboratory, concentration and time optimization were performed using a sun simulator. The optimum concentration and time for TiO_2 and ZrO_2 suspensions were discovered to be ten thousand ppm and 20 hours, respectively. PE and PP were exposed to both natural and artificial sunlight. According to 95 percent confidence, the degradation of selected polymers by ZrO_2 and TiO_2 differs significantly in both treatment settings. PE and PP samples treated with ZrO2 nanoparticle suspension deteriorated faster than PE and PP samples treated with TiO2 nanoparticle suspension. Under these test conditions, nano ZrO2 can cause more photocatalytic degradation than nano TiO2 [110].

2.18 Improved Catalytic efficiency of t-ZrO2 nanoparticles

Using a template-free hydrothermal approach, tetragonal zirconia (t-ZrO2) nanoparticles were effectively produced and characterized using multiple measuring techniques. 99 percent of the MO had been degraded within 50 minutes. Due to successful electron hole pair separation, EIS examination of produced t-ZrO2 nanoparticles revealed a tiny semicircle, indicating greater photocatalytic activity. The high crystallinity, quantity of oxygen vacancies, bigger surface area, larger pore volume, and decrease in band gap energy due to smaller crystallite size are all factors that contribute to photocatalytic activity [112].

2.19 As a Visible-Light Photocatalyst, Fe-Doped Zirconium Titanate

The sol-gel and impregnation approaches were used to successfully manufacture iron-doped zirconium titanate. Iron-doped zirconium titanate ($ZrTiO_4$) was synthesized and characterized as a potential visible-light-responsive photocatalyst. The effects of different iron dopant concentrations and calcination temperatures on the properties of Fe-doped $ZrTiO_4$ were investigated. As a precursor, titanium tetra-iso-prop oxide (TTIP) was embedded on zirconia fine powder. Iron (II) sulphate heptahydrate ($FeSO_47H_2O$) was used to introduce a certain amount of iron 1 to 9 weight percent into the photocatalyst system. At 500 °C, photocatalysts with varying iron concentrations were calcined. $ZrTiO_4$ containing 5% iron was calcined at two different temperatures 700 and 900 °C. EDX analysis confirmed the presence of iron on the surface of $ZrTiO_4$. After 500 °C calcination, the iron content of Fe-doped $ZrTiO_4$ with the lowest bandgap (2.83 eV) is 7% [113].

2.20 The Influence of CeO_2 Advancement on ZrO_2 Nanoparticle Catalytic Performance

To improve the sono catalytic performance of ZrO_2 nanoparticles, they adopted an ultrasonic aided technique to promote CeO_2 into ZrO_2 nanoparticles. The synthesized materials' sono-catalytic activity was tested using sono-degradation of methylene blue (MB) under ultrasonic irradiation. According to the findings, adding a small amount of CeO_2 to ZrO_2 nanoparticles enhanced their efficiency in degrading MB. The highest degradation of MB was achieved at a molar ratio of 0.3:1. Among numerous reactive species, including holes, electrons, and hydroxyl radicals, holes were revealed to be the principal reactive species with a substantial function in degrading MB [115].

2.21 Ag-doped ZrO_2 diesel soot oxidation

The hydrothermal method was used to create Ag-doped ZrO_2 nanoparticles (NPs) for diesel soot oxidation. The soot oxidation temperature of ZrO_2 NPs and Ag-doped ZrO_2 NPs increased and reduced with increasing sintering temperature, respectively. Adjusting the sintering temperature for the soot oxidation reaction improves the thermal stability of Ag-doped ZrO_2 NPs catalysts. A low-containment Ag-doped ZrO_2 with a novel technique will be given to conserve precious metal levels in particulate matter (PM) treatment systems [117].

Chapter 3

Experimental Work

I have synthesized graphene oxide, reduced graphene oxide, pure zirconia silver doped zirconia with different mass ratios and then characterized them. I have also synthesized composites of rGO with 0.04 % silver doped zirconia with 1:1, 1:2 and 1:3 respectively. In this section I will explain the procedure of their synthesis.

3.1 Graphene Oxide Synthesis (GO)

Graphene oxide was synthesized by oxidizing graphite using a modified Hummer's method. [41].

3.1.1 Materials

The chemicals for the synthesis of GO are as follow which are used without any further purification:

· Graphite

· Sodium Nitrate ($NaNO_3$)

· Sodium Permanganate ($KMnO_4$)

· Sulfuric Acid (H_2SO_4)

· Hydrogen Peroxide (H_2O_2)

· Deionized Water

3.1.2 Procedure

2 g of graphite was placed in an ice bath in a beaker with 50 mL of sulfuric acid. A stirrer and thermometer were placed in the solution, and the temperature was kept between 0 and 5 °C. The whole system was placed on a hotplate and the solution was stirred for some time. After stirring 2 g of sodium nitrate was gradually added and temperature was sustained between 0-5 °C. The solution was stirred for two hours. The ice bath was removed after 2 hours and 6 g of potassium permanganate was added. The temperature was held at 35 °C for 48 hours, and the solution was agitated. The paste changed colour from black to a brownish grey tint. After the heating was turned off, 100 ml DI water was progressively added. The tint shifted to brown as the temperature increased to 98 degrees Celsius. Then, with steady stirring, another 200 ml of water was added. The reaction was stopped at a yellowish tint after 10ml of hydrogen peroxide was added. The mixture was allowed to settle. Then 5-10 ml of 10 percent hydrochloric acid was added. Graphene oxide settled down. The upper layer was decanted. To keep the pH at 5, it was centrifuged several times at 4000 rpm with deionized water. It was then dried in a vacuum oven at 50 °C and stored. Figure 11 depicts the entire procedure.

3.2 Reduced Graphene Oxide Synthesis (rGO)

By the chemical reduction of hydrazine hydrate RGO is synthesized [42].

3.2.1 Materials

Graphene oxide, Hydrazine hydrate, methanol and deionized water

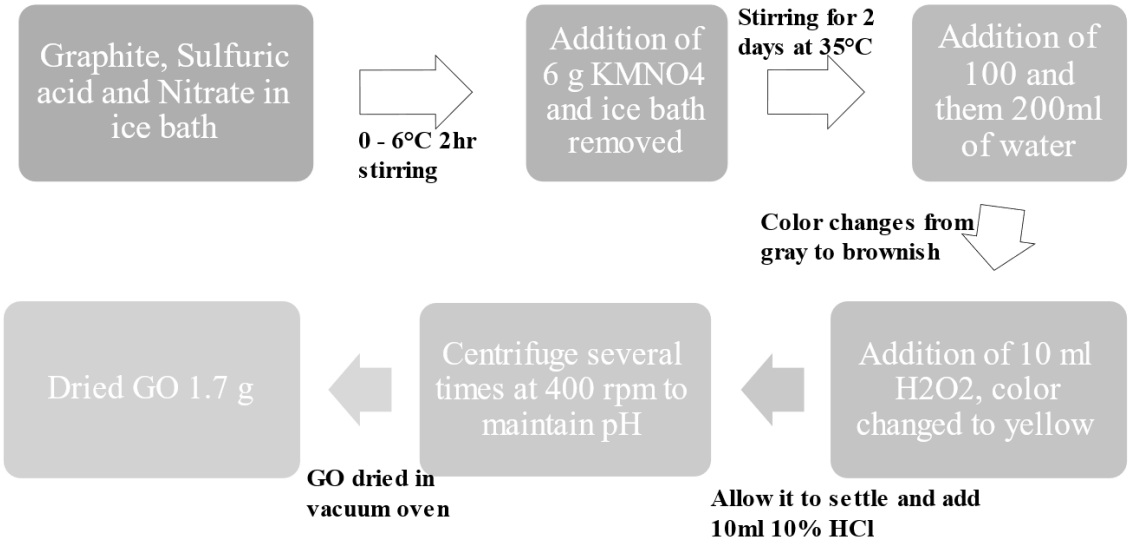

Figure 11: Schematic representation of graphene oxide synthesis.

3.2.2 Procedure

In a conical flask, 100 mg or 0.1 g of GO was added to 100 ml of DI water and sonicated for 2 hours. The homogeneous dispersion obtained after sonication was added to a round bottom flask and refluxed in an oil bath. The temperature was kept constant at 100 °C. Then 1ml of hydrazine hydrate was added and solution was kept under reflux for 24 hours. The product appeared as black solid chunks was filtered. Product was then washed with 10ml methanol and 10 ml H2O. The obtained product was dried in a vacuum oven at 50 °C for 24 hours. RGO was collected and stored after drying (figure 12).

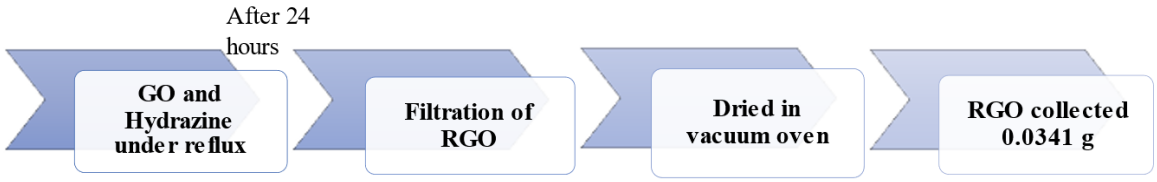

Figure 12: Schematic representation of reduced graphene oxide synthesis.

3.3 Synthesis of Zirconia (ZrO_2)

3.3.1 Materials

- Zirconium nitrate, Zr $(NO_3)_4.5H_2O$
- Ammonium hydroxide NH_4OH 25 %
- Ethanol
- Deionized water

ZrO_2 was prepared by simple hydrothermal method. Initially 0.01M aqueous solution of zirconium nitrate was prepared. The mixture was stirred for 1 h for homogenization. Following that, 25 percent ammonium hydroxide was added dropwise to the mixture while it was constantly stirred. After 1 hour, the white zirconium precipitates were collected and transferred to a Teflon-lined autoclave. The precipitates were hydrothermally treated for 24 hours at 180 °C. The precipitates were centrifuged and washed numerous times with water and ethanol. To make powdered ZrO_2, the washed precipitates were dried in a vacuum oven at 80 °C.

3.4 Synthesis Ag doped ZrO_2

3.4.1 Materials

- Zirconium nitrate, Zr $(NO_3)_4.5H_2O$
- Ammonium hydroxide NH_4OH 25 %
- Ethanol
- Deionized water
- $AgNO_3$

A simple hydrothermal method was used to create Ag-doped ZrO_2. A 0.01M aqueous solution of zirconium nitrate was first prepared and mixed with a 0.1mM aqueous solution of silver nitrate. For homogenization, the mixture was stirred for 1 hour. Following that, 25 percent ammonium hydroxide was added dropwise to the mixture while it was constantly stirred. After one hour, the white precipitates of silver doped zirconium were collected and transferred to a Teflon-lined autoclave. The precipitates were hydrothermally treated for 24 hours at 180 °C. The precipitates were centrifuged and washed numerous times with water and ethanol. To make powdered nanocomposite, the washed precipitates were dried in a vacuum oven at 80 °C. The same experiment was repeated by increasing the precursor concentration of silver to get a series of Ag-doped ZrO_2 composite.

3.5 Synthesis Ag$_x$$ZrO_2$/Rgo

3.5.1 Materials

- Zirconium nitrate, Zr $(NO_3)_4.5H_2O$
- Ammonium hydroxide NH_4OH 25 %

- Ethanol
- Deionized water
- $AgNO_3$
- GO

The procedure was repeated for Ag doped ZrO_2/rGO till the formation white precipitates of silver doped zirconium. After that, the GO solution was combined with white precipitates and hydrothermally treated for 24 hours at 180 °C. The dark precipitates were centrifuged and washed numerous times with water and ethanol. To make powdered nanocomposite, the washed precipitates were dried in a vacuum oven at 80 °C.

3.6 Characterization

X-ray diffraction (XRD, USPCASP) was utilized to characterize the pure material, doped material, and nanocomposites for crystalline structure and phase composition. Cu K radiation was used as the X-ray source, which was operated at 45 kV and 100 mA. Scanning electron microscopy and Energy Dispersive X-Ray Analysis (EDX) were employed to study the morphology and check the elemental composition of the as manufactured material (SEM, PINSTEC Nano SEM 450, FEI-Thermo Fisher Scientific). UV-Vis diffuse reflectance spectroscopy in the wavelength range of 200-800 nm was used to determine the photocatalyst's absorbance (SNS Lambda 650S, PerkinElmer, USA). A fluorescence spectrophotometer (Fluoromate FS-2, SCINCO, South Korea) fitted with a 150 W Xe arc lamp (200–900 nm) was used to capture photoluminescence (PL SNS) spectra at ambient temperature. SNS employed Fourier Transform Infrared Spectroscopy (FTIR) to identify the functional groups in the as synthesized material.

3.7 Photocatalytic Degradation test

The photocatalytic degradation activity of the as-prepared nanocomposite was investigated at various methyl orange (MO) solution pH levels. The experiment was conducted under UV light irradiation with a 500 W UV lamp with a specific wavelength of 420 nm and a light intensity of 100 mW cm^{-2}. To achieve adsorption-desorption equilibrium, the prepared photocatalyst ($Ag_{0.04}ZrO_2$/rGO) (10 mg) was dispersed in 1000 mL of the MO aqueous solution (10 ppm) (0.03mM) and stirred at 25-degree Celsius room temperature in the dark for 30 minutes. After exposing the reaction mixture to visible light for 20 minutes, 5 mL of an aliquot was taken at each 20-minute interval to record absorbance with a UV-vis spectrophotometer.

Chapter 4

Results and Discussion

4.1 X-Ray crystallography (XRD)

XRD results of dopped samples (ZrO_2: $Ag_{0.01}$, ZrO_2: $Ag_{0.02}$, ZrO_2: $Ag_{0.03}$, ZrO_2: $Ag_{0.04}$, ZrO_2: $Ag_{0.05}$) are shown in figure 13. All the XRD pattern's similar to that of ZrO_2 and no peak has been observed for Ag doping. This is assuring intrinsic doping of Ag into the zirconia crystals Fig. A show the XRD pattern of the Ag dopped zirconia with different mass ratios demonstrate definite diffraction peaks(2Ɵ) agrees to the monoclinic phase of ZrO_2 at 17.5° (100), 24.3°(110), 28.3°(-111), 31.5°(111), 34.3°(020), 40.7°(-211), 50.3°(220), 58.2°(-222), 63°(311), 65.9°(-231) characteristics crystal planes respectively and matches with the JCPDS file No. 65-1023. The only difference between the XRD patterns is the decrease in intensity of a characteristic peak of Zirconia at 28.3°, with the increase in the amount of Ag. This shows that pure ZrO_2 is in crystalline form and crystallinity decreases with increasing amount of Ag. These results also have good agreement with the SEM results.

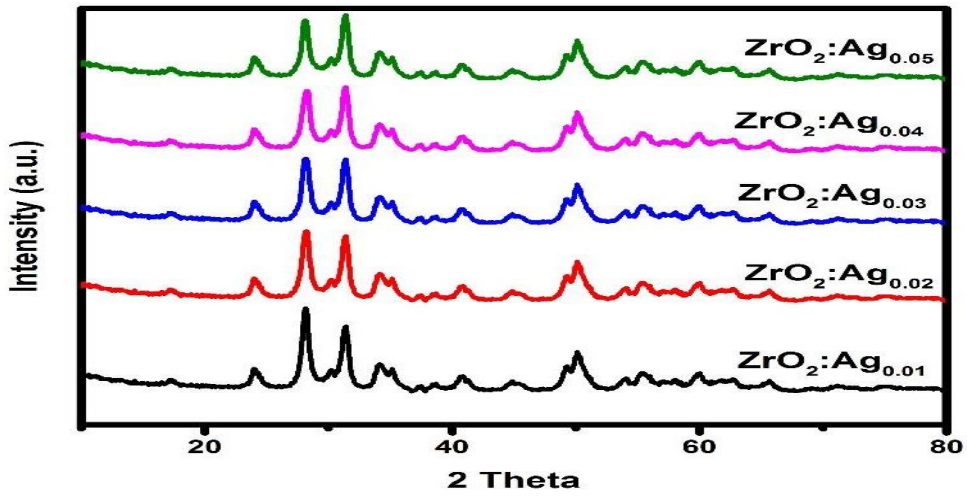

Figure 13. XRD pattern of AgxZrO$_2$ (x=0.01-0.05).

4.1.1 Comparison of X-Ray crystallography (XRD)

Figure 14 shows XRD patterns of pure ZrO$_2$, ZrO$_2$: Ag$_{0.04}$ and composite Ag$_{0.04}$@ZrO$_2$/rGO all the sample's showed Ag is intrinsically dopped into the interstices of ZrO$_2$, due to which catalytic activity

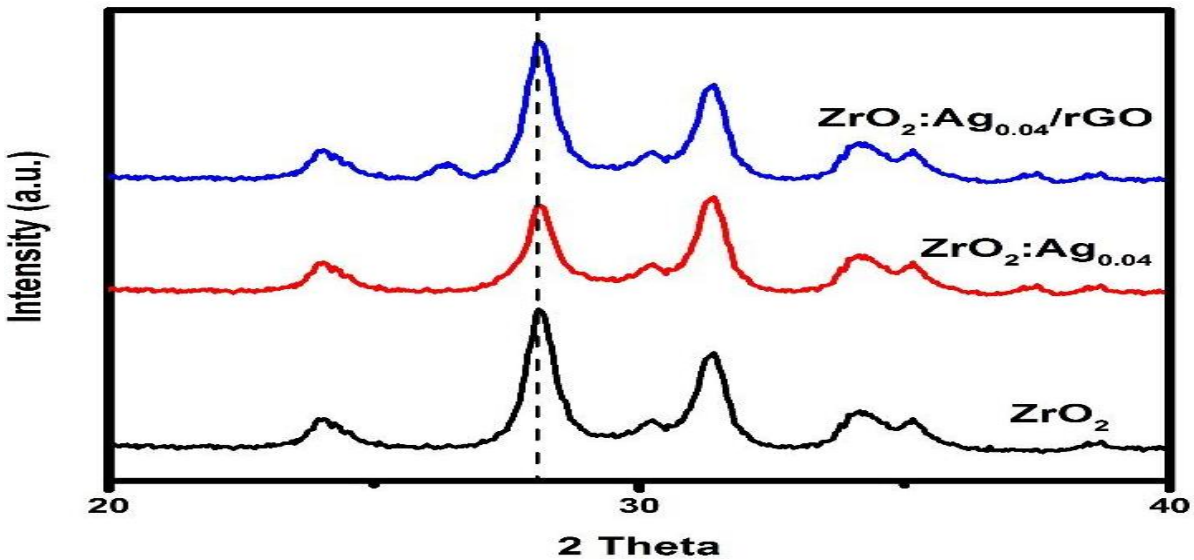

Figure 14: Comparison of XRD of Ag0.04ZrO$_2$ and Ag0.04ZrO$_2$/rGO with pure ZrO$_2$.

of the material improved significantly. It's clear from the figure below that the peak at 28.3°

4.2 SEM Micrographs

One of the most important aspects of solution-processed synthesis for achieving the required morphology of $AgZrO_2$/rGO nanocomposite is optimizing the doping and composite concentrations. Figure 15 depicts SEM micrographs of pure ZrO_2 (a-d). In the case of pure ZrO_2, the growing film has network-like structures with vast voids of thick rods **(Figure 15(a)).** When the dopant Ag concentration is increased to 0.4 mM, the cavities in the film change into a dense network of pores, which aid photocatalytic activity by increasing surface area (Figure 16 (b)). When rGO is added to Ag doped ZrO2, densely packed nanorods are formed that are aligned vertically on the porous surface **(Figure 17(d))**.

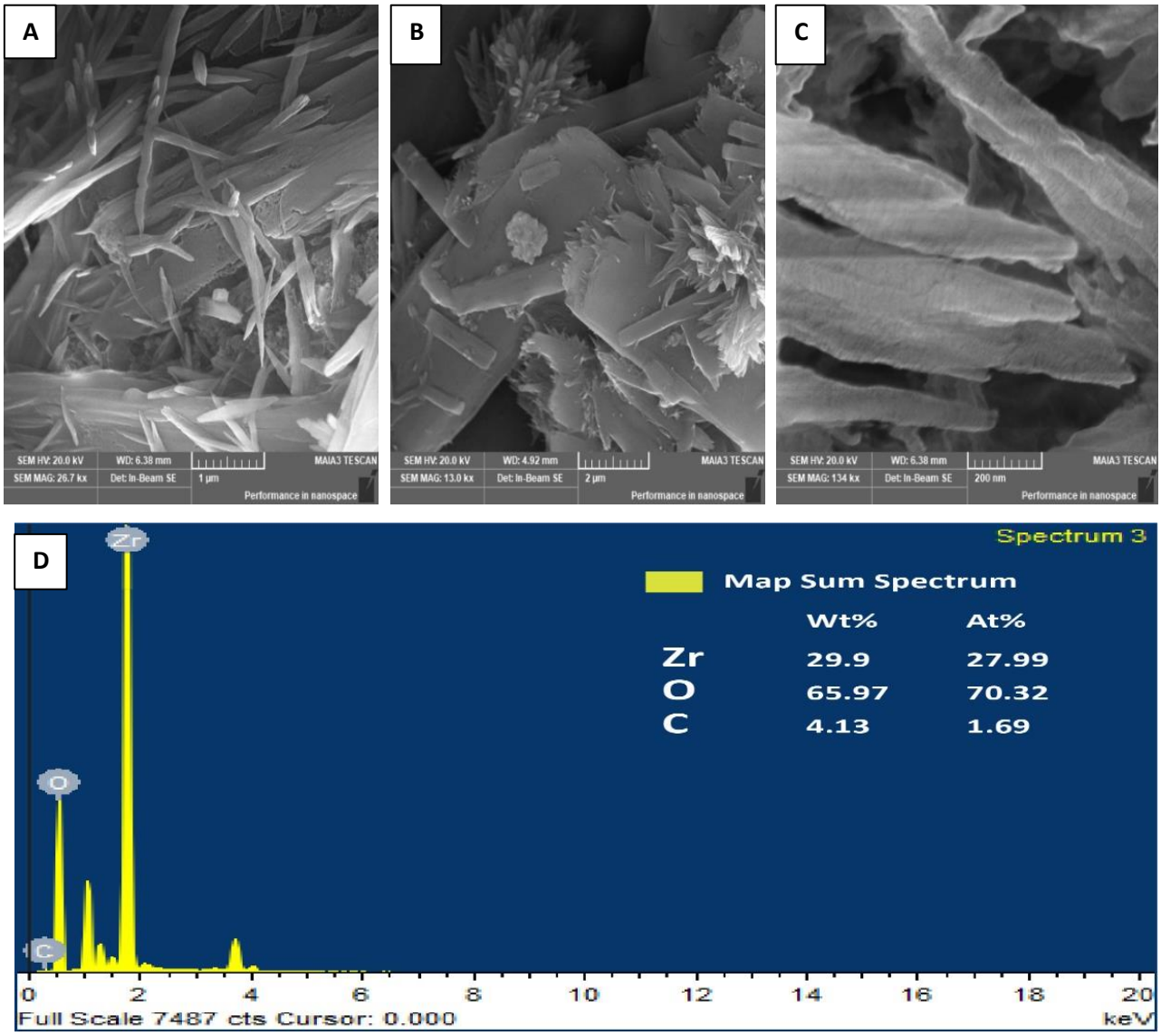

Figure 15: Scanning electron micrograph of ZrO_2 (a-c) EDX ZrO_2(d).

The average diameter of the nanorods is 100 nm. Because of the high surface-to-volume ratio, this form of surface morphology has electrocatalytic advantages. The $AgZrO_2$/rGO nanorods' wide network structure can increase active sites for photocatalytic reactions while also providing channels for electrolyte diffusion during the intercalation/de-intercalation phase. As shown in Figure 13(e), EDX analysis was used to determine the chemical composition of $AgZrO_2$/rGO nanorods. The spectra

show the presence of O, Ag, Zr and C with atomic percentage of 49.68, 3.19, 21.27 and 25.86, respectively.

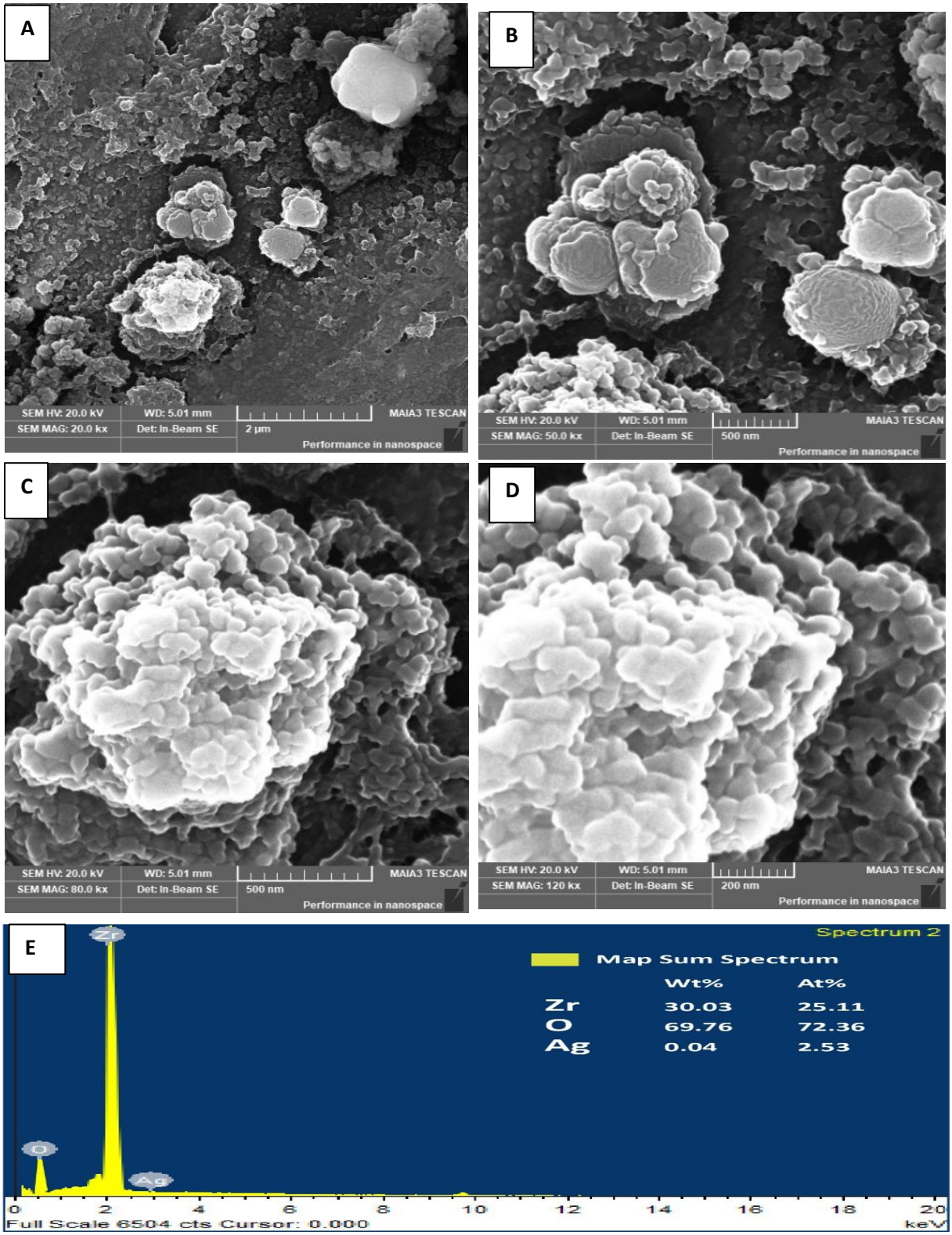

Figure 16: Scanning electron micrograph of $Ag0.04ZrO_2$ (a-d) EDX of $Ag0.04ZrO_2$(e).

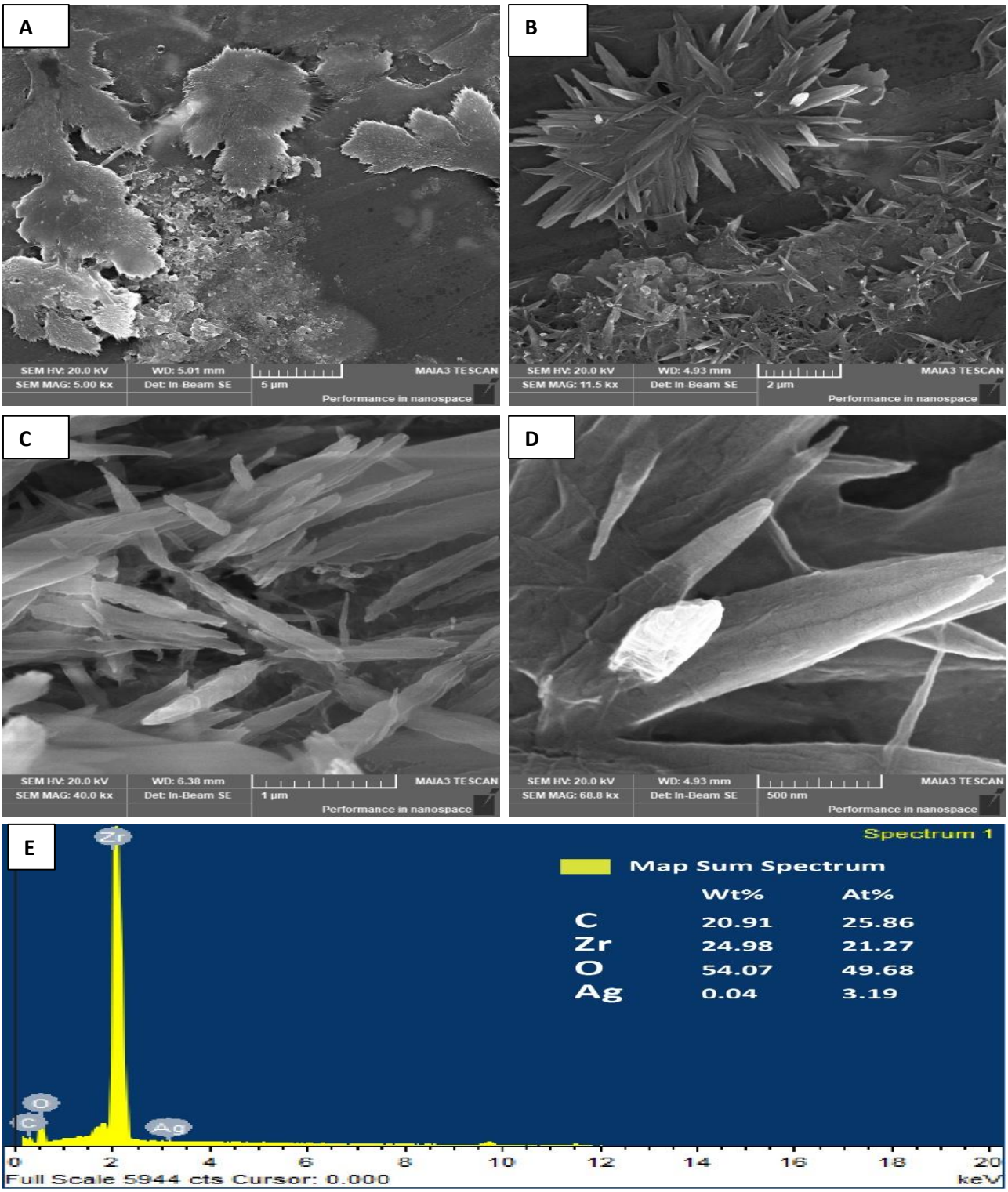

Figure 17: Scanning electron micrograph of Ag0.04ZrO$_2$/rGO (a-d) EDX of Ag0.04ZrO$_2$/rGO (e).

4.3 UV-Vis diffuse reflectance spectroscopy

Figure 14 depicts the UV spectra of as synthesized materials. As can be seen in Figure 14c, high bandgap absorption energy in the UV region was needed for ZrO_2. Ag0.04@ZrO_2 exhibits moderate visible and heavy UV absorption with an absorption edge around 420 nm. The integration of Ag0.04@ZrO_2 into rGO increased the adsorption of visible light overall. Photocatalytic activity in the visible region is depicted by the improved shift in absorption of Ag0.04@ZrO_2/rGO [118].

The bandgap energy of the synthesised photocatalyst was calculated using the Tauc equation [119]:

$$(h\nu\alpha)1/n = A\,(h\nu - Eg)$$

where h is Planck's constant, v is vibrational frequency, is absorption coefficient, Eg is bandgap energy, A is a proportionality constant, and n is kind of electron transfer (n = 1/2 for directly allowed transitions). The Kubelka– Munk function (F(R∞)) has a value that is directly proportional to. [120]:

where h is Planck's constant, v is vibrational frequency, α is absorption coefficient, Eg is bandgap energy, A is proportionality constant, and n is form of electron transfer (n = 1/2 for directly permitted transitions). As shown in [120], the value of is directly proportional to the Kubelka– Munk function

$$(F(R\infty)):\ (h\nu F(R\infty))^2 = A\,(h\nu - Eg)$$

The Tauc plot shown in the insets of Figure 18 shows bandgap energy by the projection of the tangent on the x-axis to the turning point of curvature.

The bandgap energies of ZrO_2, $Ag_{0.04}@ZrO_2$, and $Ag_{0.04}@ZrO_2$/rGO are 3.48, 3.11, and 2.99 eV, respectively. Incorporation of Ag as dopants lowered the bandgap energy of $Ag_{0.04}@ZrO_2$ (3.11 eV) while the addition of rGO further lowered the band gap of $Ag_{0.04}@ZrO_2$/rGO inferring the photocatalytic activity of composite in visible light. The absorbance and reflectance of the as synthesized catalyst are also shown in the figure 18, which reveals that pure zirconia has a high band gap energy as compared to the doped and composite photocatalysts. That is why by adding Ag as a

dopant the band gap energy decreases in doped as well as in composite which enhance the photocatalytic activity by decreasing band gap energy.

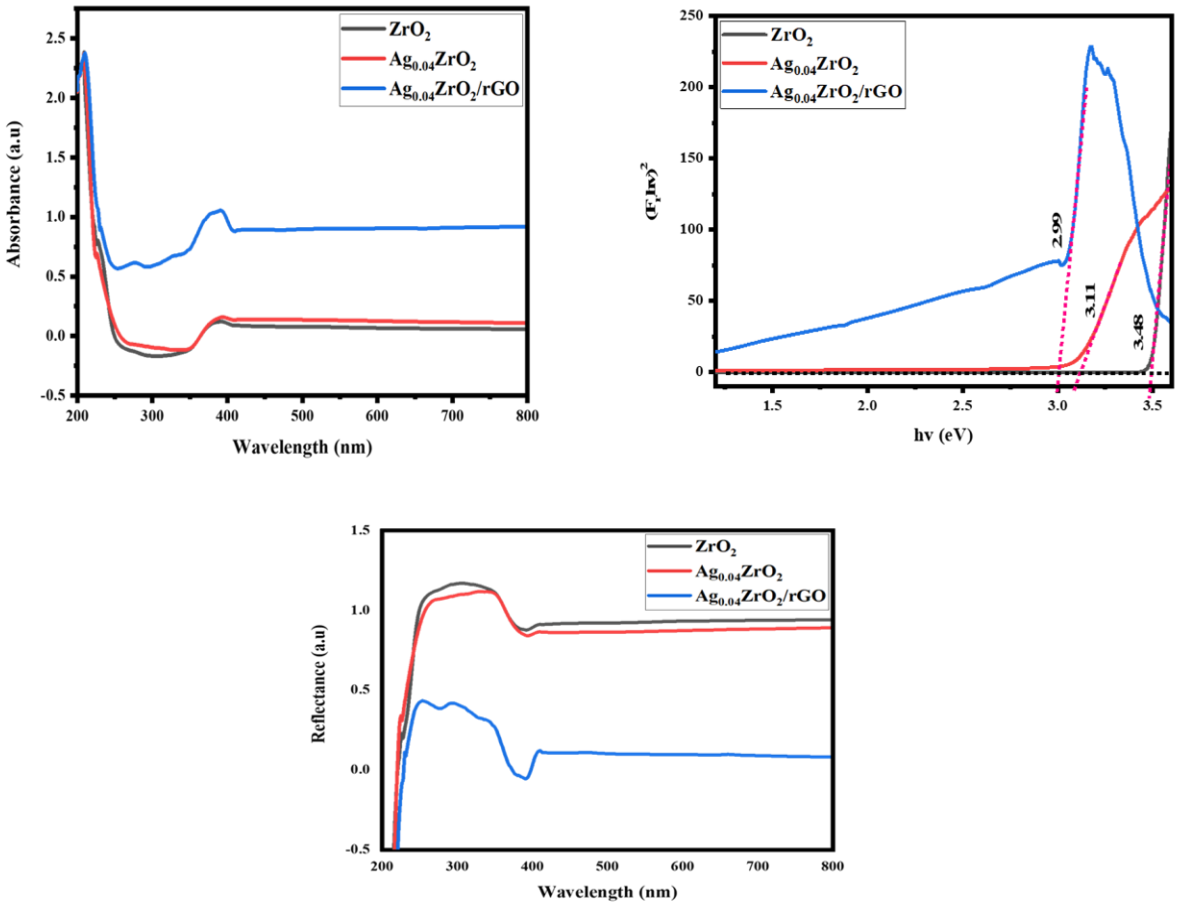

Figure 18: UV-DRS spectra of (a) ZrO_2 (b) Ag0.04@ZrO_2 (c) Ag0.04@ZrO_2/rGO.

4.4 Photoluminescence analysis of the composites

Photoluminescence can be used to investigate the isolation and conversion of photogenerated electrons and holes in photocatalyst heterojunctions (PL). Figure 19 shows the excitation spectra of

Ag0.04@ZrO_2/rGO composites, which display lambda max at 325 nm. Near-band-edge transitions and oxygen vacancies may be responsible for the shorter and longer wavelength emission of ZrO_2 and its composites, respectively. Interfacial charge transfer from Ag0.04@ZrO_2 to rGO could explain the redshift in the spectrum of Ag0.04@ZrO_2/rGO. In the Ag0.04@ZrO_2/rGO spectrum, this alternative transfer pathway causes PL quenching [121], [122]. Since the intensity is in the order ZrO_2 > Ag0.05@ZrO_2 > Ag0.04@ZrO_2 > Ag0.04@ZrO_2/rGO, ZrO_2 > Ag0.05@ZrO_2 > Ag0.04@ZrO_2 > Ag0.04@ZrO_2/rGO the charge carriers in Ag0.04@ZrO2/rGO are thought to be well separated, resulting in higher photocatalytic activity.

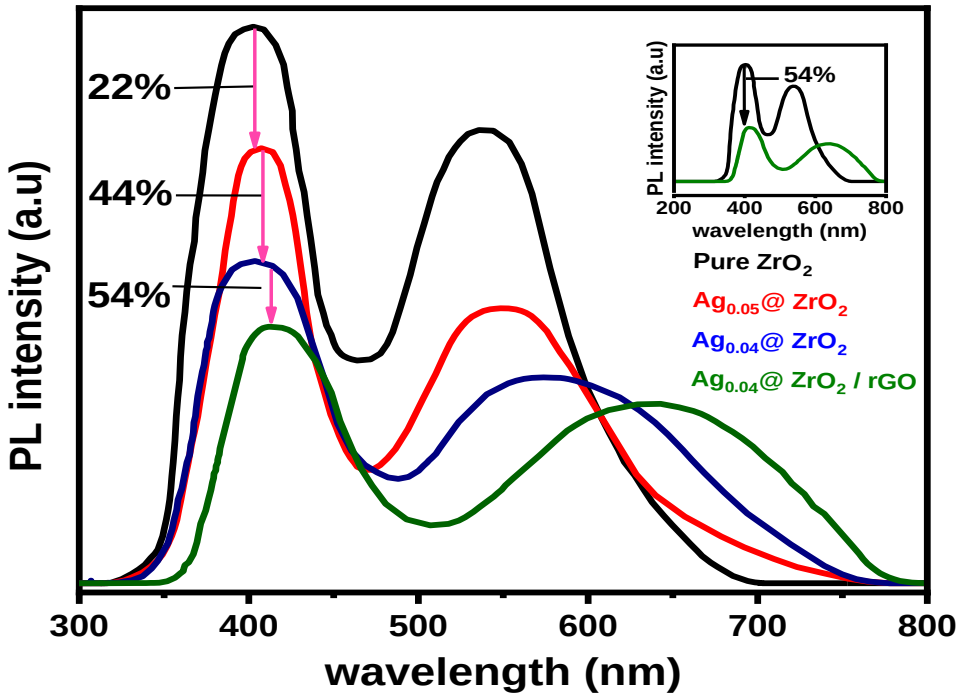

Figure 19: Photoluminescence spectra ZrO_2 composites.

4.5 Fourier Transform Infrared Spectroscopy (FTIR)

FTIR spectroscopy were used to identify chemical bonds as well as functional groups in the as synthesized material by producing an infrared absorption spectrum. Here in this study, we synthesized pure ZrO_2, Ag doped ZrO_2 and the composite of doped material with rGO and then characterize through FTIR spectroscopy. In figure 20 we compare the FTIR spectra of pure ZrO_2 and $Ag_{0.04}ZrO_2$. In this figure both the FTIR spectras shown the peak around 559 cm^{-1} and 700 cm^{-1} arises from the Zr-O vibrations of the tetragonal zirconia and monoclinic zirconia respectively. Thus, we can say that here we synthesize mixed monoclinic and tetragonal ZrO_2. In addition, there is certain peaks in the spectra of $Ag_{0.04}ZrO_2$ at around 3323 cm^{-1} due to the stretching and bending vibration of hydroxyl groups (OH), which is due to moister absorption of the material. The band around 1430 cm^{-1} and 1500 cm^{-1} is due to the absorption of non-bridging hydroxyl (OH) group. In figure 21 the FTIR spectra of $Ag_{0.04}ZrO_2$/rGO with (1:1) is shown. In this spectrum the sharp peak around 561 cm^{-1} is arises due to the Zr-O vibrations in the zirconia. The broad peak around 1007 cm^{-1} and 1578 cm^{-1} is due to the bending and stretching vibrations of the C-C bonds. The broad peak at around 2170 cm^{-1} is due to the stretching vibration of C=C bonds. This is clear from this spectrum that reduced graphene oxide and $Ag_{0.04}$ ZrO_2 heterojunction is formed which will improve the photocatalytic activity of the material.

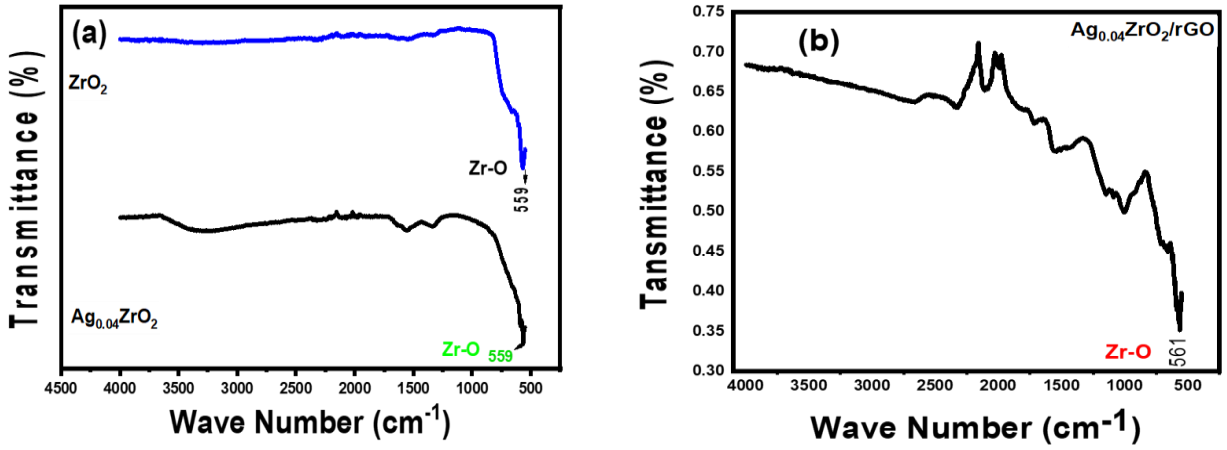

Figure 20:FTIR Spectra of pure ZrO_2 and $Ag0.04ZrO_2$ (a) FTIR Spectra of $Ag0.04ZrO_2$/rGO (1:1) (b).

4.6 Photocatalytic activity

Through the photodegradation of MO dye under UV light irradiation, the photocatalytic activities of undoped ZrO_2, Ag-doped ZrO_2 with different Ag percentages, and $Ag0.04@ZrO_2$/rGO composites with 1:1, 1:2, and 1:3 were compared. As the holes react with water and produce $OH^{\bullet}$ radicals, the organic contaminants are oxidized. As conduction band electrons react with oxygen, superoxide anion radicals (O^{-2}) are formed, resulting in the reduction of pollutants. Under UV irradiation, these redox reactions are capable of destroying organic contaminants. Figure 21 a show the absorption spectra of methyl orange MO with ZrO_2 Ag-doped ZrO_2 with different Ag ratios. It is clearly indicating there is no noticeable shift in absorbance of methyl orange while it is kept in the dark, but after regular interval of times the absorbance decreases indicating the degradation of MO. Figure 21 b showing the comparison of MO degradation with bare ZrO_2, $Ag0.04@ZrO_2$/rGO composites with a 1:1, 1:2, 1:3 respectively. It clearly indicates that in the absence of a stimulus, there

is no discernible shift in absorbance. MO absorption spectra were observed at 0, 20, 40, 60, 80, and 100 minutes in the presence of undoped ZrO_2 Ag0.04@ZrO_2/rGO composites with 1:1, nano powders, as shown in Figs. a–c. In all cases, the intensity of the MO absorption peak decreases as the irradiation period increases. The following formula was used to measure the photocatalytic degradation efficiencies of composite materials/nano powders: [123]

$$\textbf{Degradation efficiency (\%)} = ((A_0 - A)/A_0)\ 100$$

where A_0 is the absorbance of MO solution before irradiation and A is the absorbance after irradiation. Figure 21 c indicating the MO degradation efficiency is found to be 26%, 60%, and 87 percent for undoped ZrO_2 Ag-doped ZrO_2 Ag0.04@ZrO_2/rGO composites with 1:1 nanopowders after 100 minutes of irradiation, respectively. The higher degradation efficiency of Ag0.04@ZrO_2/rGO is due to improved electron mobility, increased specific surface area, and higher adsorption. The large surface area of rGO sheets aids in the decomposition process [124]. Organic pollutant degradation is favored by graphene-based semiconductor photocatalysts. Previous research has shown that doping Ag and rGO into ZrO_2 nanoparticles can improve their photocatalytic activity, resulting in excellent photocatalytic degradation of MO [125-127].

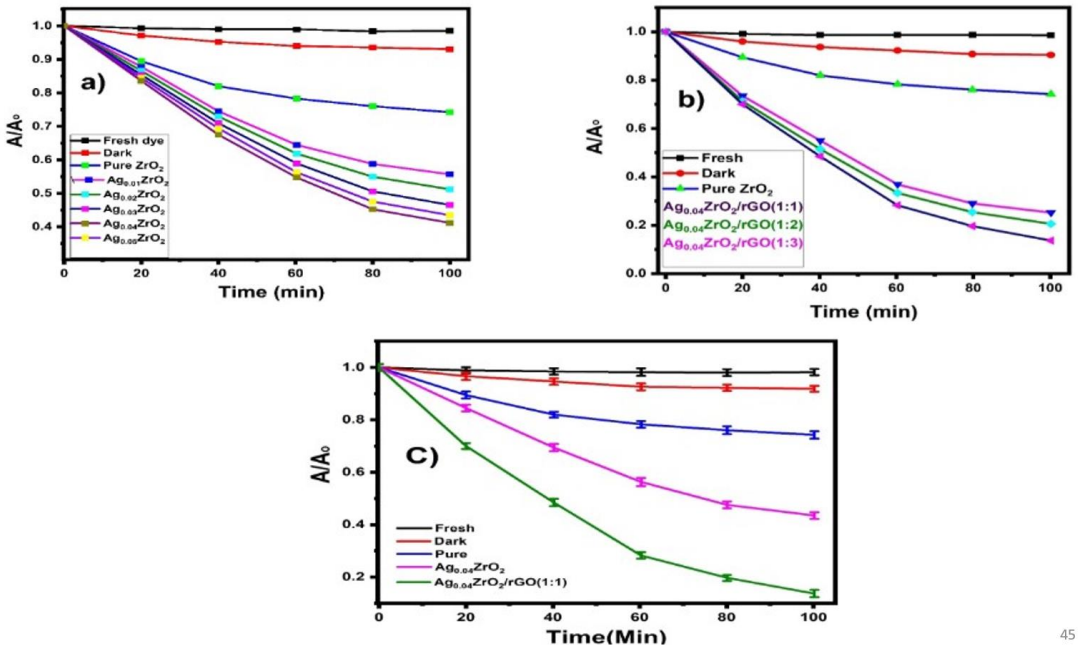

Figure 21: Comparison of degradation of MO (a)ZrO_2 andAg_xZrO_2 (x = 0.01-0.05) (b) ZrO_2 and $Ag_{0.04}ZrO_2$/rGO (1:1-1:3) (c) ZrO_2, $Ag_{0.04}ZrO_2$ and $Ag_{0.04}ZrO_2$/rGO.

4.6.1 Bar Graphs of Different Photocatalysts for Degradation of MO

The bar diagram (Figure 22) clearly shows that as silver doping increases, degradation efficiency increases dramatically. When we compare ZrO_2 with Ag_xZrO_2 (X=0.01-0.05) the degradation efficiency increases from pure ZrO_2 to $Ag_{0.04}ZrO_2$ than decreases for $Ag_{0.05}ZrO_2$ in red bar graphs. When we compare ZrO_2 with $Ag_{0.04}ZrO_2$/rGO with 1:1,1:2 and 1:3 instead of pure zirconia $Ag_{0.04}ZrO_2$/rGO with 1:1 shows maximum degradation up to 87% in 100 min showing in blue. In short pure zirconia degrade MO up to 26% in 100 min, in case of doped photocatalysts $Ag_{0.04}ZrO_2$ degrade MO up to 60% that's is why this photocatalysts is chosen for composite formation. In case of composites $Ag_{0.04}ZrO_2$/rGO with 1:1 shows 87 % degradation in 100 min.

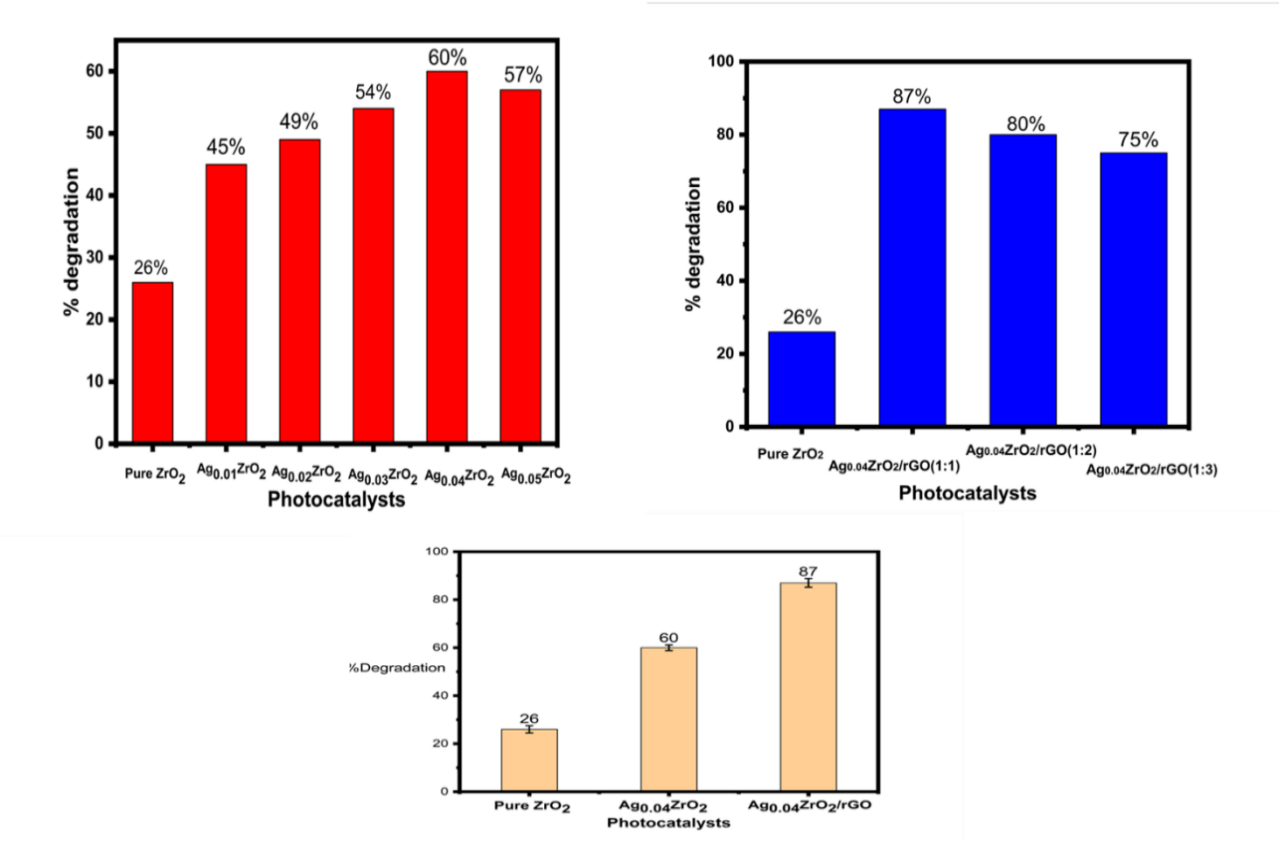

Figure 22: Bar Graphs Showing the % Degradation of MO through different photocatalysts.

4.7 Kinetic Studies

The photocatalytic degradation is governed by a pseudo-first-order kinetic reaction, with the following kinetics:

$\ln (Ao/At) = k\,t$

The reaction rate constant is k, and the reaction time is t. The slope of the straight line is used to measure the deterioration rate constant (k). Figure 23 c showing the kinetic simulations of $Ag_{0.04}ZrO_2$/rGO with 1:1 that has higher degradation rate constant (0.0204) than doped $Ag_{0.04}ZrO_2$ (0.00871) and undoped ZrO_2 (0.00289).

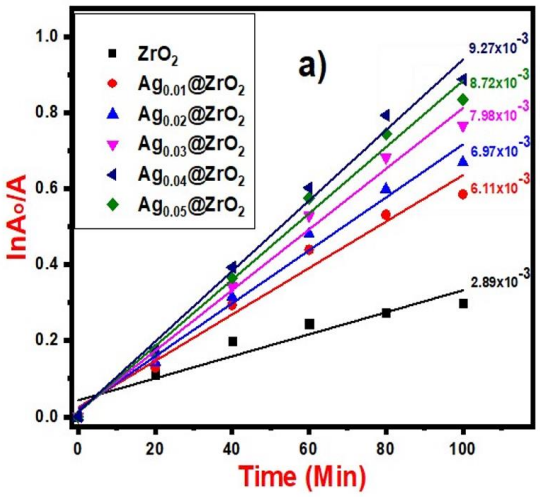

Equation	y = a + b*x					
Weight	No Weightin					
Residual Sum of	0.00552	0.00665	0.00541	0.00484	0.00579	0.00596
Pearson's r	0.95594	0.9875	0.99213	0.9946	0.9946	0.9950
Adj. R-Squar	0.89228	0.9689	0.9804	0.9865	0.9865	0.9877
		Value	Standard Err			
pure	Intercept	0.0432	0.02689			
	Slope	0.0028	4.4406E-4			
Ag0.1	Intercept	0.0245	0.0295			
	Slope	0.0061	4.8718E-4			
0.2	Intercept	0.0196	0.02662			
	Slope	0.0069	4.39577E-4			
0.3	Intercept	0.0139	0.02517			
	Slope	0.0079	4.15599E-4			
0.5	Intercept	0.0117	0.02754			
	Slope	0.0087	4.54755E-4			
0.4	Intercept	0.0123	0.02794			
	Slope	0.0092	4.61491E-4			

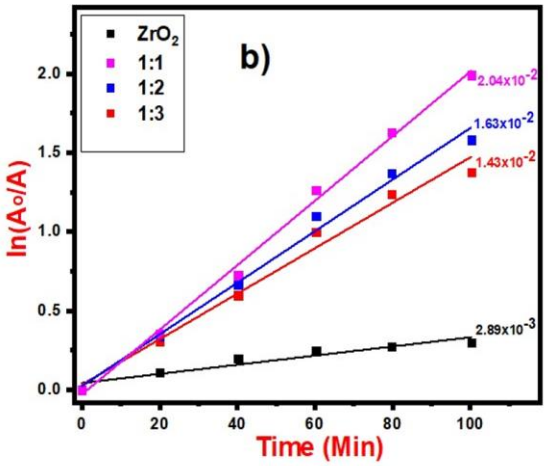

Equation	y = a + b*x			
Weight	No Weighting			
Residual Sum of Squares	0.00547	0.02326	0.01698	0.01124
Pearson's r	0.9564	0.99207	0.99548	0.99808
Adj. R-Square	0.89337	0.98026	0.98873	0.99521
		Value	Standard Erro	
Pure	Intercept	0.04305	0.02677	
	Slope	0.00289	4.41583E-4	
1:3	Intercept	0.03249	0.05523	
	Slope	0.01438	9.10911E-4	
1:2	Intercept	0.02424	0.04719	
	Slope	0.01632	7.78324E-4	
1:1	Intercept	-0.02855	0.03839	
	Slope	0.02041	6.33228E-4	

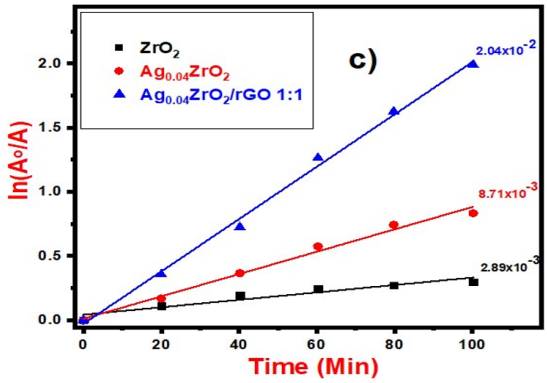

		Value	Error	R^2
ZrO_2	Intercept	0.043	0.026	0.89
-	Slope	0.002	$4.4E^{-4}$	
$Ag_{0.04}ZrO_2$	Intercept	0.011	0.027	0.98
-	Slope	0.008	$4.5E^{-4}$	
$Ag_{0.04}ZrO_2$/rGO	Intercept	-0.028	0.038	0.99
-	Slope	0.020	$6.3E^{-4}$	

Figure 23: Kinetic Simulation of pure by ZrO_2, $Ag0.04ZrO_2$ and $Ag0.04ZrO_2$/rGO (1:1).

Due to higher degradation rate constant of $Ag_{0.04}ZrO_2$/rGO with 1:1 photocatalyst degrade MO up to 87% in 100 min of irradiation in photochemical reactor. The kinetic simulation is also done with different doped samples and with the composites in figure 23 a and b respectively.

4.8 UV absorption spectra of MO

The UV spectra of methyl orange degradation are shown in this figure by ZrO_2, Ag_XZrO_2 where X=0.01 to 0.05 and $Ag_{0.04}ZrO_2$/rGO 1:1,1:2 and 1;3. There is no shift in the absorption peaks in all the spectra's when the the MO solution is placed in the dark with no photocatalyst. When the photocatalyst is added into the methyl orange solution and placed in the dark there is a slight shift in the absorbance peak due to the establishment of adsorption desorption equilibria. Then the MO solution were placed in photochemical reactor for 100 min. After each 20 min interval the aliquot is taken out and record its absorption spectra by using UV-Vis spectrophotometer. There is a regular decrease in the absorption spectrum of MO up to 100 min of time interval. After 100 min pure ZrO_2 degrade MO up to 26 %, $Ag_{0.04}ZrO_2$ Degrade MO up to 60% (best among all doped samples) and $Ag_{0.04}ZrO_2$/rgo (1:1) up to 87% (best among all composites) at 3 pH which is highest among all the other catalysts. Here I show those absorbance graphs which shows degradation of MO orange up to 100 min of time interval. The first graph in the figure below shows the degradation of MO with pure ZrO_2 while the next five graphs showing the degradation of MO with $AgxZrO_2$ X=0.01 to 0.05. Last four graphs showing the degradation of MO with $Ag_{0.04}ZrO_2$/rGO with 1:1, 1:2 and 1:3.

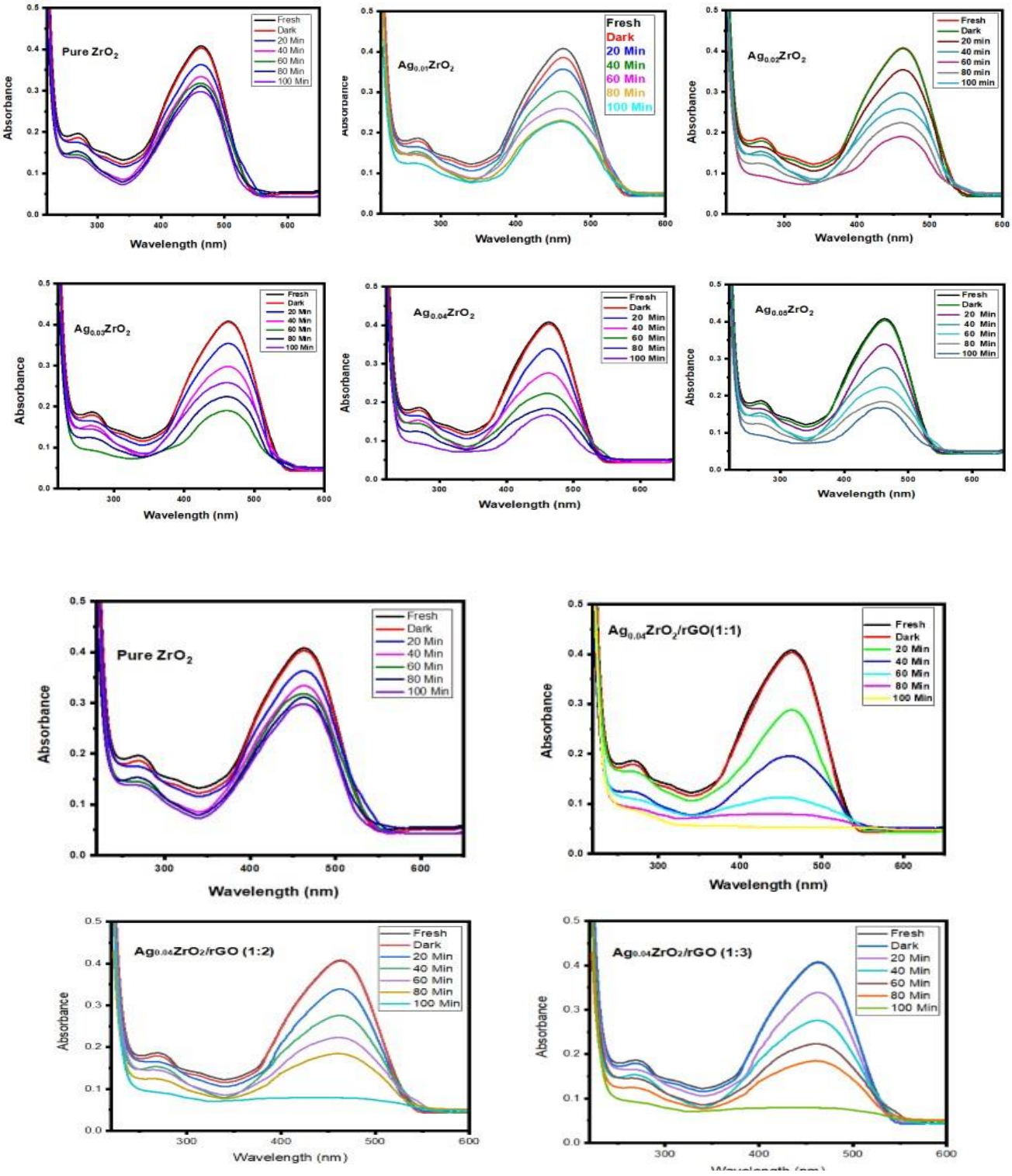

Figure 24: UV Spectra of MO degradation with pure ZrO_2, Ag$_x$$ZrO_2$ X=0.01 to 0.05 and its composite with rGO.

4.9 Effect of pH on photocatalytic performance

The pH of the stream, the composition of the dye, and the ability to absorb onto the photocatalyst surface all play a part in photocatalysis because it is a surface phenomenon. Depending on whether the environment is acidic or caustic, the catalyst's surface is charged positively or negatively. The photocatalyst's zero-point charge (ZPC) affects its ability to receive charges, which is why zirconia particles become positively or negatively charged as the pH of the solution changes. [128]. The ZPC values for ZrO_2 vary from 5.5 to 6.4, depending on the synthesis process. [128-130]. As a result, at pH values less than pH ZPC, the surface becomes positively charged (due to H+ ions), whereas at pH values greater than pH ZPC, the surface becomes negatively charged (due to H+ ions) (attributed to OH-) [130-132].

In acidic settings, MO, on the other hand, is resistive to creating a quinone structure. A distinct colour change as well as an absorbance peak shift were detected at lower pH values, indicating the presence of a quinone structure in MO. The sulfonic groups (-SO3-) aid hydrogen uptake and increase the hydrophobicity of the catalyst surface, making the quinone structure more oxidation resistant than the azo structure. [133] MO molecules have been converted to a quinone structure, which means they are now a new substance with a distinct breakdown process. As a result, we limited our investigation to pH 1 to 11 in this study. The solution's pH was changed as indicated in the experiment section, but the reaction was left unregulated. As indicated in Fig. 9a, dye degradation is greatest from neutral pH to acidic pH (3.0) to more acidic settings. The rise in fractional conversion with an increase in pH can explain the production of hydroxyl radicals during the reaction ($OH^- + h \rightarrow OH\bullet$). At a lower pH, the hydroxyl radicals are scavenged more slowly, allowing them to react with the dye more readily. The catalyst is no more stable at pH 2 and 1 thus we limit our study up to these pH values.

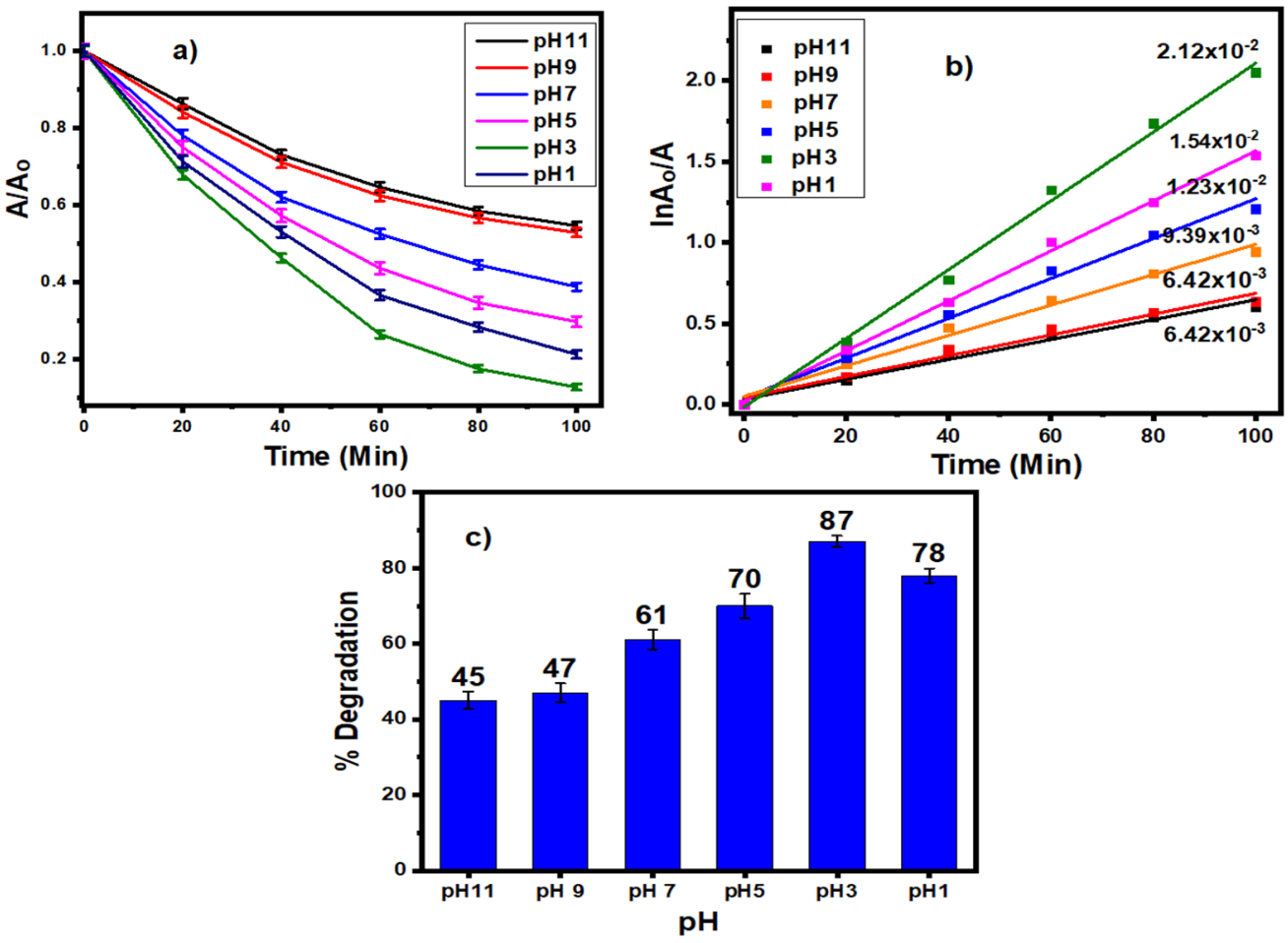

Figure 25: Comparison of degradation of MO at various pH (a) Kinetic simulation of photocatalytic degradation of MO (c) Bar graph of % degradation at various pH.

4.10 Effects of dosage of catalyst

To investigate the impact of catalyst quantity on the removal of MO by $Ag_{0.04}@ZrO_2$/rGO, a sequence of 5, 10, and 15 mg/100ml catalyst dosages were chosen. The removal rate increases as the $Ag_{0.04}@ZrO_2$/rGO dose is increased, as shown in Fig 10. However, it's worth noting that the removal rate first increased as the catalyst dosage was increased, then decreased as the catalyst dosage was increased more. When a catalyst is overdosed, the opacity of the suspension increases, blocking light

penetration and rendering the shadowed catalyst particles ineffective at producing radicals. In other words, as the dosage is increased, the mechanism gradually transforms from an optically dilute to an optically dense system due to light shortage [134].

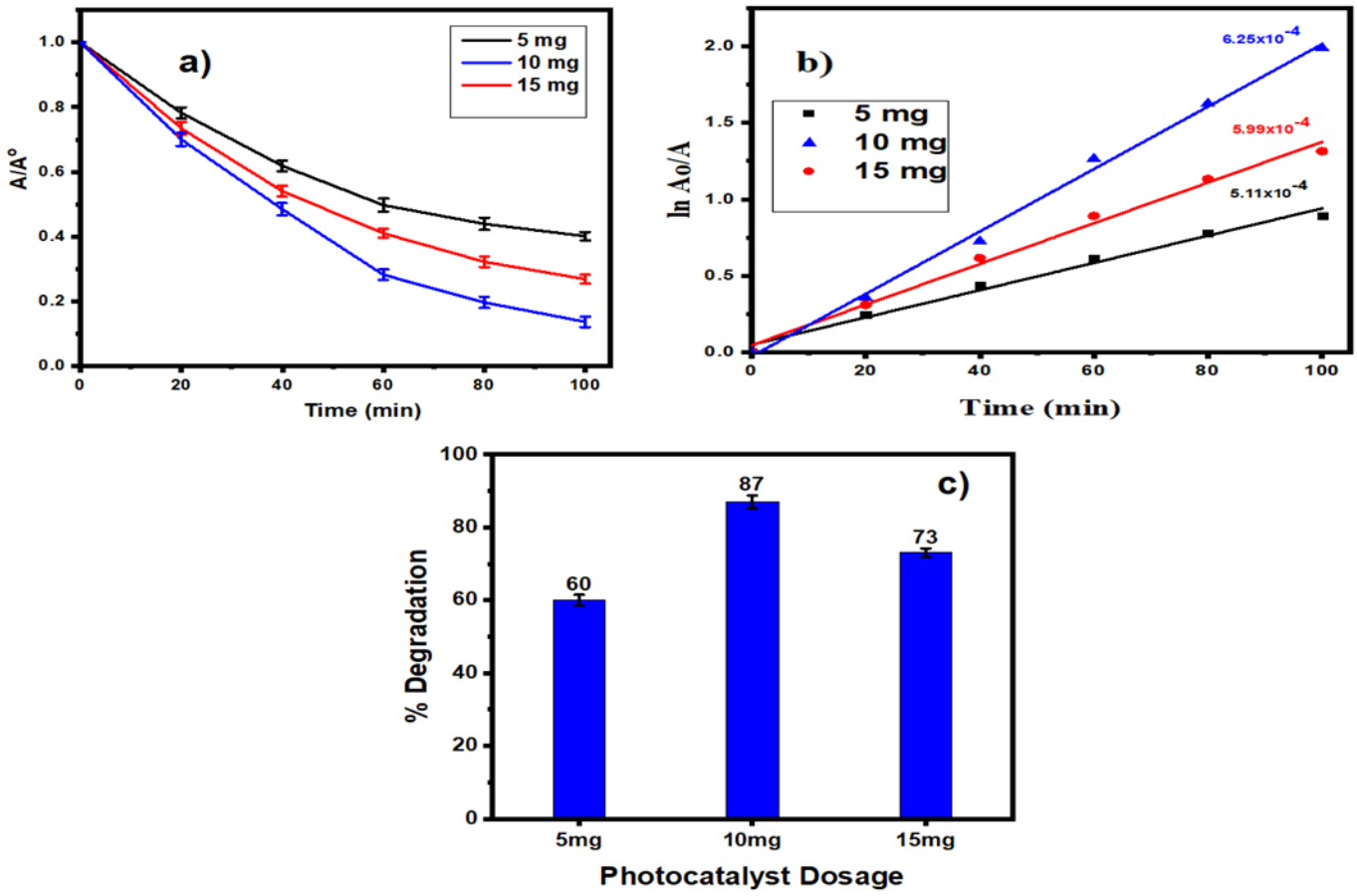

Figure 26: Comparison of degradation of MO at different dosage (a) Kinetic simulation of photocatalytic degradation of MO (c) Bar graph of % degradation at different dosage.

4.11 Reusability and Stability

The reusability and photostability of the as synthesized catalyst were checked carefully. For the application of photocatalyst, especially doped catalyst composites with photosensitive and unstable components like Ag, reusability and stability are critical. Five repeated experiments using a recycled doped ZrO_2 and its composite/ photocatalyst demonstrated the photostability of $Ag0.04@ZrO_2$/rGO composites for MO degradation. For five repeated tests, the photocatalyst show high visible light photostability, but there is a small decrease in photocatalytic activity from 87 percent to 78 percent degradation, respectively, when compared to the first-run result. This is might be due to the loss of some of the catalyst during recovery or due to the decrease in the efficiency.

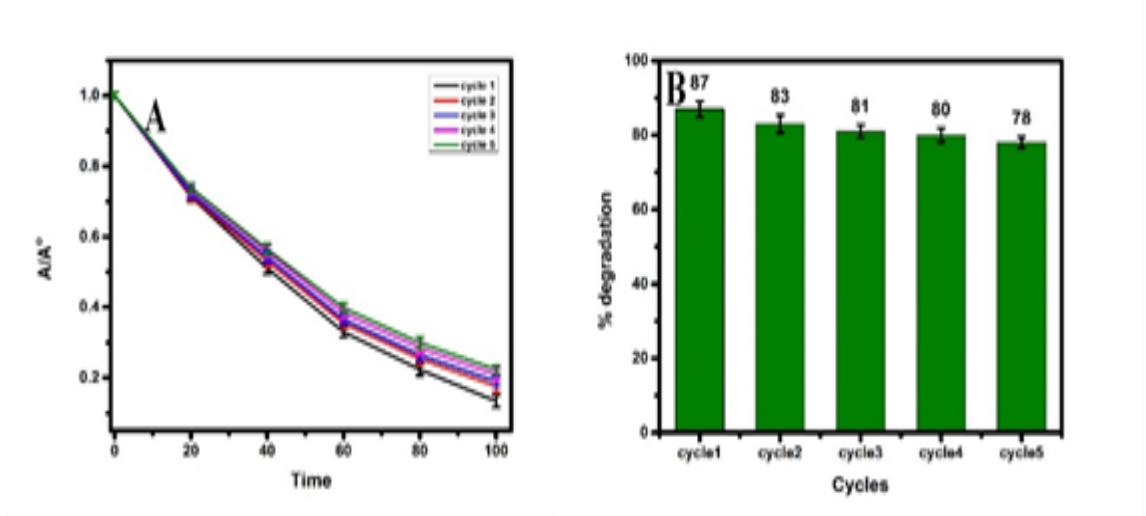

Figure 27: Reusability of $Ag0.04ZrO_2$/rGO up to 5 cycles (B) Bar graph of recycling.

4.12 Mott–Schottky plots

In Figure 29 the Mott-Schottky plots of Ag doped ZrO_2 and rGO are shown. These plots are used to calculate the flate band potential (Efb). The slop of Mott-Schottky plots of $Ag_{0.04}ZrO_2$ (-0.32V against Ag/AgCl) is higher than that of rGO (-0.82V vs Ag/AgCl), indicating that $Ag_{0.04}ZrO_2$ is n-type and

rGO is p-type. For the degradation of MO, this verifies the establishment of an efficient p-n junction between $Ag_{0.04}ZrO_2$ and rGO. Due to the formation of this p-n junction $Ag_{0.04}ZrO_2$/rGO with 1:1 shows the maximum results for MO degradation.

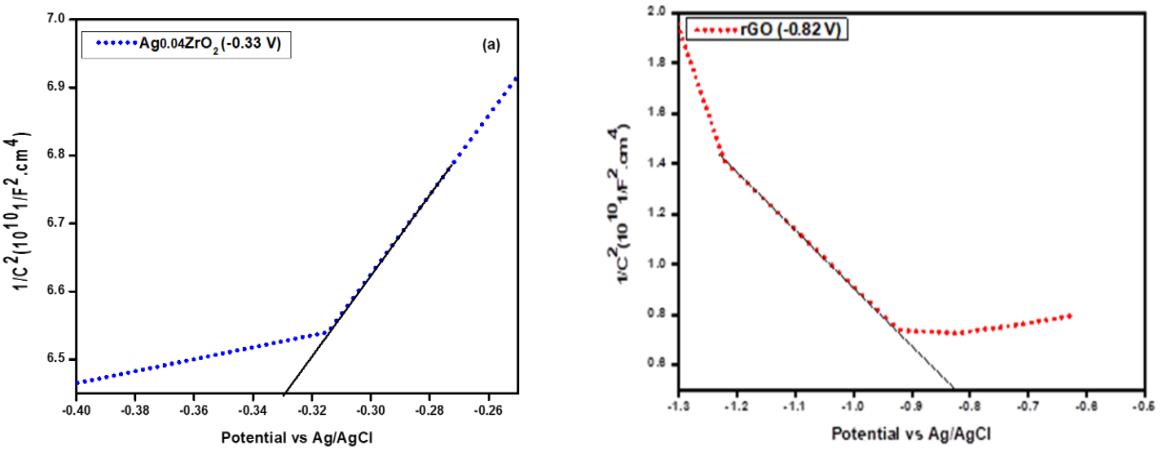

Figure 28: Mott-Schottky plots of Ag doped ZrO_2 and rGO.

4.13 Mechanisms for photocatalytic degradation of MO

The band gap energy, as well as the potential of the valence and conduction bands, are crucial components in determining the mechanism of the degradation process. From Mott-Schottky plots, the conduction band potential was predicted to be -0.12 eV against RHE for Ag0.04ZrO2 and -0.62 eV vs RHE for rGO. The band gap energies for $Ag_{0.04}ZrO_2$ and rGO were computed using the Tauc plot and found to be 3.11 eV for Ag0.04ZrO2 and 1.69 eV for rGO. VB=CB + Eg was used to compute the potential of the valence band of $Ag_{0.04}ZrO_2$ (2.99 eV) and rGO (1.07 eV).

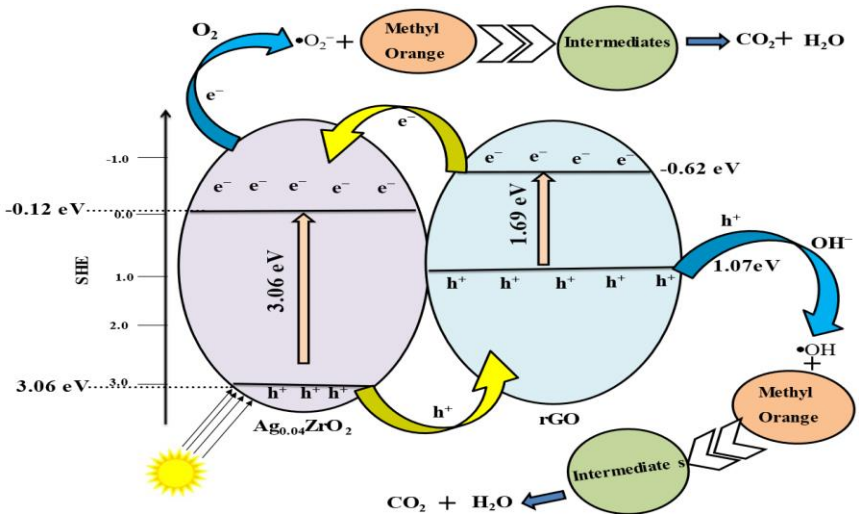

Figure 29: Mechanisms for photocatalytic degradation of MO.

Chapter 5

Conclusion

We have successfully synthesized pure Zirconia, Ag doped Zirconia and nanocomposites of Ag-doped Zirconia with reduced graphene oxide (Ag_x ZrO_2/rGO) where x= (0.01, 0.02, 0.03, 0.04 and .05) by facile hydrothermal method. After synthesizing, these nanocomposites were investigated through SEM, EDX, XRD, and UV-DRS are some of the analytical techniques used. Scanning electron microscope (SEM) was used for morphological studies, X-ray powder Diffraction (XRD) was used for crystallographic studies, and ultraviolet Diffuse reflectance spectroscopy (UV-DRS) was used for band gap determination. Photoluminescence was used to investigate the photocatalytic behavior of the synthesized nanocomposite. In contrast to Ag0.04ZrO_2 and ZrO_2, the Ag0.04ZrO_2/rGO photocatalyst has excellent visible light absorption, allowing for effective methyl orange photocatalytic degradation. Ag0.04ZrO_2/rGO produced the highest rate of methyl orange degradation (87%) due to the low rate of electron and hole pair recombination between Ag and ZrO_2 heterojunction. The photo-assisted degradation of MO followed pseudo-first order kinetics, according to the kinetic simulation report. The Ag0.04ZrO_2/high rGO's efficiency can be attributed to heterojunction formation, porous structure, and large active surface area.

References

1. Colpini, L.M.S., et al., Discoloration and degradation of textile dye aqueous solutions with titanium oxide catalysts obtained by the sol–gel method. Dyes and Pigments, 2008. **76**(2): p. 525-529.
2. Tian, B., et al., Flame sprayed V-doped TiO2 nanoparticles with enhanced photocatalytic activity under visible light irradiation. Chemical Engineering Journal, 2009. **151**(1-3): p. 220-227.
3. Robinson, T., et al., Remediation of dyes in textile effluent: a critical review on current treatment technologies with a proposed alternative. Bioresource technology, 2001. **77**(3): p. 247-255.
4. Gnanaprakasam, A., V. Sivakumar, and M. Thirumarimurugan, Influencing parameters in the photocatalytic degradation of organic effluent via nanometal oxide catalyst: a review. Indian Journal of Materials Science, 2015. **2015**.
5. Zhou, W., et al., A newly-designed polyoxometalate-based plasmonic visible-light catalyst for the photodegradation of methyl blue. Journal of Molecular Catalysis A: Chemical, 2013. **371**: p. 70-76.
6. García-Montaño, J., et al., The testing of several biological and chemical coupled treatments for Cibacron Red FN-R azo dye removal. Journal of hazardous materials, 2008. **154**(1-3): p. 484-490.
7. Ullah, R. and J. Dutta, Photocatalytic degradation of organic dyes with manganese-doped ZnO nanoparticles. Journal of Hazardous materials, 2008. **156**(1-3): p. 194-200.
8. Ju, Y., et al., Photodegradation of malachite green using UV–vis light from two microwave-powered electrodeless discharge lamps (MPEDL-2): further investigation on products, dominant routes and mechanism. Chemical engineering journal, 2013. **221**: p. 353-362.
9. Shang, L., et al., Heteronanostructure of Ag particle on titanate nanowire membrane with enhanced photocatalytic properties and bactericidal activities. Journal of Hazardous Materials, 2010. **178**(1-3): p. 1109-1114.
10. Wahab, R., et al., Non-hydrolytic synthesis and photo-catalytic studies of ZnO nanoparticles. Chemical Engineering Journal, 2011. **175**: p. 450-457.
11. Byrappa, K., et al., Photocatalytic degradation of rhodamine B dye using hydrothermally synthesized ZnO. Bulletin of materials science, 2006. **29**(5): p. 433-438.

13. Sathishkumar, P., et al., ZnO supported CoFe2O4 nanophotocatalysts for the mineralization of Direct Blue 71 in aqueous environments. Journal of Hazardous Materials, 2013. **252**: p. 171-179.
14. Di Paola, A., et al., A survey of photocatalytic materials for environmental remediation. Journal of hazardous materials, 2012. **211**: p. 3-29.
15. Saien, J., et al., Homogeneous and heterogeneous AOPs for rapid degradation of Triton X-100 in aqueous media via UV light, nano titania hydrogen peroxide and potassium persulfate. Chemical Engineering Journal, 2011. **167**(1): p. 172-182.
16. Ananpattarachai, J., P. Kajitvichyanukul, and S. Seraphin, Visible light absorption ability and photocatalytic oxidation activity of various interstitial N-doped TiO2 prepared from different nitrogen dopants. Journal of hazardous materials, 2009. **168**(1): p. 253-261.
18. Zaleska, A., Doped-TiO2: a review. Recent patents on engineering, 2008. **2**(3): p. 157-164.
19. Shi, J.-w., J.-t. Zheng, and P. Wu, Preparation, characterization and photocatalytic activities of holmium-doped titanium dioxide nanoparticles. Journal of Hazardous Materials, 2009. **161**(1): p. 416-422.
20. Kang, M., S.-J. Choung, and J.Y. Park, Photocatalytic performance of nanometer-sized FexOy/TiO2 particle synthesized by hydrothermal method. Catalysis Today, 2003. **87**(1-4): p. 87-97.
21. Yu, J., et al., Enhanced photocatalytic activity of TiO2 powder (P25) by hydrothermal treatment. Journal of Molecular Catalysis A: Chemical, 2006. **253**(1-2): p. 112-118.
22. Sathishkumar, P., et al., CoFe2O4/TiO2 nanocatalysts for the photocatalytic degradation of Reactive Red 120 in aqueous solutions in the presence and absence of electron acceptors. Chemical engineering journal, 2013. **220**: p. 302-310.
23. Fu, P., et al., Thermal stability and microstructure characterization of MgAl2O4 nanoparticles synthesized by reverse microemulsion method. Materials Research, 2013. **16**(4): p. 844-849.
24. Fu, J., et al., Soft-chemical synthesis of mesoporous nitrogen-modified titania with superior photocatalytic performance under visible light irradiation. Chemical engineering journal, 2013. **219**: p. 155-161.
25. Soltani, T. and M.H. Entezari, Sono-synthesis of bismuth ferrite nanoparticles with high photocatalytic activity in degradation of Rhodamine B under solar light irradiation. Chemical Engineering Journal, 2013. **223**: p. 145-154.

26. Dong, F., et al., Band structure and visible light photocatalytic activity of multi-type nitrogen doped TiO2 nanoparticles prepared by thermal decomposition. Journal of Hazardous Materials, 2009. **162**(2-3): p. 763-770.
27. Song, S., et al., Influences of pH value in deposition-precipitation synthesis process on Pt-doped TiO2 catalysts for photocatalytic oxidation of NO. Journal of Environmental Sciences, 2012. **24**(8): p. 1519-1524.
28. Mai, F., et al., Mechanisms of photocatalytic degradation of Victoria Blue R using nano-TiO2. Separation and Purification Technology, 2008. **62**(2): p. 423-436.
29. Sohrabnezhad, S., A. Pourahmad, and E. Radaee, Photocatalytic degradation of basic blue 9 by CoS nanoparticles supported on AlMCM-41 material as a catalyst. Journal of Hazardous Materials, 2009. **170**(1): p. 184-190.
30. Wu, Y., et al., Preparation of nitrogen and fluorine co-doped mesoporous TiO2 microsphere and photodegradation of acid orange 7 under visible light. Chemical Engineering Journal, 2010. **162**(2): p. 710-717.
31. Barakat, N.A., et al., Influence of temperature on the photodegradation process using Ag-doped TiO2 nanostructures: negative impact with the nanofibers. Journal of Molecular Catalysis A: Chemical, 2013. **366**: p. 333-340.
32. Yousefi, A., A. Allahverdi, and P. Hejazi, Effective dispersion of nano-TiO2 powder for enhancement of photocatalytic properties in cement mixes. Construction and building materials, 2013. **41**: p. 224-230.
33. Cao, Y., et al., An enhanced visible-light photocatalytic activity of TiO2 by nitrogen and nickel–chlorine modification. Separation and Purification Technology, 2013. **104**: p. 256-262.
34. Fuerte, A., et al., Nanosize Ti–W mixed oxides: effect of doping level in the photocatalytic degradation of toluene using sunlight-type excitation. Journal of Catalysis, 2002. **212**(1): p. 1-9.
35. Asahi, R., et al., Visible-light photocatalysis in nitrogen-doped titanium oxides. science, 2001. **293**(5528): p. 269-271.
36. Rodríguez-González, V., et al., MTBE visible-light photocatalytic decomposition over Au/TiO2 and Au/TiO2–Al2O3 sol–gel prepared catalysts. Journal of Molecular Catalysis A: Chemical, 2008. **281**(1-2): p. 93-98.

37. Pouretedal, H.R., et al., Nanoparticles of zinc sulfide doped with manganese, nickel and copper as nanophotocatalyst in the degradation of organic dyes. Journal of Hazardous Materials, 2009. **162**(2-3): p. 674-681.
38. Yu, T., et al., Characterization, activity and kinetics of a visible light driven photocatalyst: cerium and nitrogen co-doped TiO2 nanoparticles. Chemical Engineering Journal, 2010. **157**(1): p. 86-92.
39. Tong, T., et al., Preparation of Fe3+-doped TiO2 catalysts by controlled hydrolysis of titanium alkoxide and study on their photocatalytic activity for methyl orange degradation. Journal of Hazardous Materials, 2008. **155**(3): p. 572-579.
40. Kumar, P.S.S., M.R. Raj, and S. Anandan, Nanoporous Au–TiMCM-41—An inorganic hybrid photocatalyst toward visible photooxidation of methyl orange. Solar energy materials and solar cells, 2010. **94**(10): p. 1783-1789.
41. Subramanian, V., E.E. Wolf, and P.V. Kamat, Catalysis with TiO2/gold nanocomposites. Effect of metal particle size on the Fermi level equilibration. Journal of the American Chemical Society, 2004. **126**(15): p. 4943-4950.
42. Zhang, Q., et al., A high efficiency microreactor with Pt/ZnO nanorod arrays on the inner wall for photodegradation of phenol. Journal of hazardous materials, 2013. **254**: p. 318-324.
43. Sobana, N., K. Selvam, and M. Swaminathan, Optimization of photocatalytic degradation conditions of Direct Red 23 using nano-Ag doped TiO2. Separation and Purification Technology, 2008. **62**(3): p. 648-653.
44. Sakthivel, S., et al., Enhancement of photocatalytic activity by metal deposition: characterisation and photonic efficiency of Pt, Au and Pd deposited on TiO2 catalyst. Water research, 2004. **38**(13): p. 3001-3008.
45. Ma, Y., et al., Synthesis and characterization of thermally stable Sm, N co-doped TiO2 with highly visible light activity. Journal of Hazardous Materials, 2010. **182**(1-3): p. 386-393.
46. Rajabi, H.R., et al., High-performance pure and Fe3+-ion doped ZnS quantum dots as green nanophotocatalysts for the removal of malachite green under UV-light irradiation. Journal of Hazardous Materials, 2013. **250**: p. 370-378.
47. Kruefu, V., et al., Photocatalytic degradation of phenol using Nb-loaded ZnO nanoparticles. Engineering Journal, 2012. **16**(3): p. 91-100.

48. Barakat, M., et al., Photocatalytic degradation of 2-chlorophenol by Co-doped TiO2 nanoparticles. Applied Catalysis B: Environmental, 2005. **57**(1): p. 23-30.
49. Ghaffari, M., et al., Synthesis and visible light photocatalytic properties of SrTi (1− x) FexO (3− δ) powder for indoor decontamination. Powder technology, 2012. **225**: p. 221-226.
50. Sakthivel, S. and H. Kisch, Daylight photocatalysis by carbon-modified titanium dioxide. Angewandte Chemie International Edition, 2003. **42**(40): p. 4908-4911.
51. Wang, H. and J.P. Lewis, Effects of dopant states on photoactivity in carbon-doped TiO2. Journal of Physics: Condensed Matter, 2005. **17**(21): p. L209.
52. Yu, J.C., et al., Effects of F-doping on the photocatalytic activity and microstructures of nanocrystalline TiO2 powders. Chemistry of materials, 2002. **14**(9): p. 3808-3816.
54. Ma, S., et al., Facile synthesis of ZnO nanorod arrays and hierarchical nanostructures for photocatalysis and gas sensor applications. Journal of hazardous materials, 2011. **192**(2): p. 730-740.
55. Zhang, X., et al., Photodegradation of acetaminophen in TiO2 suspended solution. Journal of Hazardous Materials, 2008. **157**(2-3): p. 300-307.
56. Seshadri, H., et al., Photocatalytic degradation of liquid waste containing EDTA. Desalination, 2008. **232**(1-3): p. 139-144.
57. Venkatachalam, N., et al., Enhanced photocatalytic degradation of 4-chlorophenol by Zr4+ doped nano TiO2. Journal of Molecular Catalysis A: Chemical, 2007. **266**(1-2): p. 158-165.
58. Liang, C.-H., et al., The effect of erbium on the adsorption and photodegradation of orange I in aqueous Er3+-TiO2 suspension. Journal of hazardous materials, 2006. **138**(3): p. 471-478.
59. Zhang, J., et al., Investigations of TiO2 photocatalysts for the decomposition of NO in the flow system: the role of pretreatment and reaction conditions in the photocatalytic efficiency. Journal of Catalysis, 2001. **198**(1): p. 1-8.
60. Sun, H., et al., Visible-light-driven TiO2 catalysts doped with low-concentration nitrogen species. Solar Energy Materials and Solar Cells, 2008. **92**(1): p. 76-83.
61. Li, F., et al., Photodegradation of an azo dye using immobilized nanoparticles of TiO2 supported by natural porous mineral. Journal of Hazardous Materials, 2008. **152**(3): p. 1037-1044.
62. Karunakaran, C. and R. Dhanalakshmi, Semiconductor-catalyzed degradation of phenols with sunlight. Solar energy materials and solar cells, 2008. **92**(11): p. 1315-1321.

63. Prado, A.G. and L.L. Costa, Photocatalytic decouloration of malachite green dye by application of TiO2 nanotubes. Journal of hazardous materials, 2009. **169**(1-3): p. 297-301.
64. Jalil, A.A., N. Sapawe, and S. Triwahyono, Photodecolorization of methylene blue over EGZrO2/EGZnO/EGFe2O3/HY photocatalyst: Effect of radical scavenger. Malaysian Journal of Fundamental and Applied Sciences, 2013. **9**(2).
65. Shie, J.-L., et al., Photodegradation kinetics of formaldehyde using light sources of UVA, UVC and UVLED in the presence of composed silver titanium oxide photocatalyst. Journal of Hazardous materials, 2008. **155**(1-2): p. 164-172.
66. Saleh, T.A., et al., Enhancement in photocatalytic activity for acetaldehyde removal by embedding ZnO nano particles on multiwall carbon nanotubes. Chemical engineering journal, 2011. **166**(1): p. 407-412.
67. Karimi, L., S. Zohoori, and M.E. Yazdanshenas, Photocatalytic degradation of azo dyes in aqueous solutions under UV irradiation using nano-strontium titanate as the nanophotocatalyst. Journal of Saudi Chemical Society, 2014. **18**(5): p. 581-588.
68. Shao, R., et al., Preparation and characterization of magnetic core–shell ZnFe2O4@ ZnO nanoparticles and their application for the photodegradation of methylene blue. Chemical engineering journal, 2013. **217**: p. 185-191.
69. Liu, S., et al., Graphene facilitated visible light photodegradation of methylene blue over titanium dioxide photocatalysts. Chemical Engineering Journal, 2013. **214**: p. 298-303.
70. Singhania, A. and S.M. Gupta, Nanocrystalline ZrO2 and Pt-doped ZrO2 catalysts for low-temperature CO oxidation. Beilstein Journal of Nanotechnology, 2017. **8**(1): p. 264-271.
71. Navio, J., et al., Preparation and physicochemical properties of ZrO2 and Fe/ZrO2 prepared by a sol− gel technique. Langmuir, 2001. **17**(1): p. 202-210.
72. Tan, G.-L. and X.-J. Wu, Electronic conductivity of a ZrO2 thin film as an oxygen sensor. Thin Solid Films, 1998. **330**(2): p. 59-61.
73. Chu, Y., et al., A new method for improving the ion conductivity of anion exchange membranes by using TiO 2 nanoparticles coated with ionic liquid. RSC advances, 2016. **6**(99): p. 96768-96777.
74. Guerra-Que, Z., et al., Silver nanoparticles supported on zirconia–ceria for the catalytic wet air oxidation of methyl tert-butyl ether. RSC advances, 2017. **7**(6): p. 3599-3610.

75. Li, S.-y., et al., Methyl-viologen modified ZnO nanotubes for use in electrochromic devices. RSC advances, 2016. **6**(76): p. 72037-72043.
76. Maia, T.A. and E.M. Assaf, Catalytic features of Ni supported on CeO 2–ZrO 2 solid solution in the steam reforming of glycerol for syngas production. RSC Advances, 2014. **4**(59): p. 31142-31154.
77. Tamura, M., et al., Cu sub-nanoparticles on Cu/CeO2 as an effective catalyst for methanol synthesis from organic carbonate by hydrogenation. ACS Catalysis, 2016. **6**(1): p. 376-380.
78. Bai, X., et al., Uniformly distributed anatase TiO2 nanoparticles on graphene: Synthesis, characterization, and photocatalytic application. Journal of alloys and compounds, 2014. **599**: p. 10-18.
79. Farghali, A., et al., Preparation, decoration and characterization of graphene sheets for methyl green adsorption. Journal of alloys and compounds, 2013. **555**: p. 193-200.
80. Hasanpour, F., M. Teimouri, and A. Eghbali, Electroanalysis of Bentazon Residues in Salvia Officinalis Extract Essential Oils Using ZnFe2O4 Anchored on Reduced Graphene Oxide Nanoparticles Modified Electrode. Biquarterly Iranian Journal of Analytical Chemistry, 2018. **5**(2): p. 56-61.
81. Yan, W., et al., A novel 3D structured reduced graphene oxide/TiO 2 composite: synthesis and photocatalytic performance. Journal of Materials Chemistry A, 2014. **2**(10): p. 3605-3612.
82. Yang, J., et al., Photocatalytic activities of heterostructured TiO2-graphene porous microspheres prepared by ultrasonic spray pyrolysis. Journal of alloys and compounds, 2014. **584**: p. 180-184.
83. Sher Shah, M.S.A., et al., Green synthesis of biphasic TiO2–reduced graphene oxide nanocomposites with highly enhanced photocatalytic activity. ACS applied materials & interfaces, 2012. **4**(8): p. 3893-3901.
84. Zhang, J., et al., Graphene encapsulated hollow TiO 2 nanospheres: efficient synthesis and enhanced photocatalytic activity. Journal of Materials Chemistry A, 2013. **1**(11): p. 3752-3756.
85. Li, L., et al., Template-free synthesis and photocatalytic properties of novel Fe2O3 hollow spheres. The Journal of Physical Chemistry C, 2007. **111**(5): p. 2123-2127.
86. Pan, J.H., et al., Self-etching reconstruction of hierarchically mesoporous F-TiO2 hollow microspherical photocatalyst for concurrent membrane water purifications. Journal of the American Chemical Society, 2008. **130**(34): p. 11256-11257.

87. Yu, J., W. Liu, and H. Yu, A one-pot approach to hierarchically nanoporous titania hollow microspheres with high photocatalytic activity. Crystal growth and design, 2008. **8**(3): p. 930-934.
88. Cardona, M. and Y.Y. Peter, Fundamentals of semiconductors. 2005: Springer.
89. Navío, J., et al., ZrO2 SiO2 mixed oxides: surface aspects, photophysical properties and photoreactivity for 4-nitrophenol oxidation in aqueous phase. Journal of Molecular Catalysis A: Chemical, 1996. **109**(3): p. 239-248.
90. Yu, J.C., J. Lin, and R.W. Kwok, Ti1-x Zr x O2 Solid Solutions for the Photocatalytic Degradation of Acetone in Air. The Journal of Physical Chemistry B, 1998. **102**(26): p. 5094-5098.
91. Sekulić, J., et al., Influence of ZrO2 addition on microstructure and liquid permeability of mesoporous TiO2 membranes. Microporous and mesoporous materials, 2004. **72**(1-3): p. 49-57.
92. Wyrwalski, F., et al., Bulk and surface structures of iron doped zirconium oxide systems: Influence of preparation method. Journal of materials science, 2005. **40**(4): p. 933-942.
93. Sahoo, C., A. Gupta, and A. Pal, Photocatalytic degradation of Methyl Red dye in aqueous solutions under UV irradiation using Ag+ doped TiO2. Desalination, 2005. **181**(1-3): p. 91-100.
94. Zhou, W., et al., Multi-modal mesoporous TiO2–ZrO2 composites with high photocatalytic activity and hydrophilicity. Nanotechnology, 2007. **19**(3): p. 035610.
95. Tahir, M.N., et al., Facile synthesis and characterization of monocrystalline cubic ZrO2 nanoparticles. Solid State Sciences, 2007. **9**(12): p. 1105-1109.
96. Farhadi, S. and S. Sepahvand, Na4W10O32/ZrO2 nanocomposite prepared via a sol–gel route: A novel, green and recoverable photocatalyst for reductive cleavage of azobenzenes to amines with 2-propanol. Journal of Molecular Catalysis A: Chemical, 2010. **318**(1-2): p. 75-84.
97. Polisetti, S., P.A. Deshpande, and G. Madras, Photocatalytic activity of combustion synthesized ZrO2 and ZrO2–TiO2 mixed oxides. Industrial & engineering chemistry research, 2011. **50**(23): p. 12915-12924.
98. Armatas, G.S., G. Bilis, and M. Louloudi, Highly ordered mesoporous zirconia-polyoxometalate nanocomposite materials for catalytic oxidation of alkenes. Journal of Materials Chemistry, 2011. **21**(9): p. 2997-3005.
99. Manivasakan, P., et al., Synthesis of monoclinic and cubic ZrO2 nanoparticles from zircon. Journal of the American Ceramic Society, 2011. **94**(5): p. 1410-1420.

100. Pouretedal, H., Z. Tofangsazi, and M. Keshavarz, Photocatalytic activity of mixture of ZrO2/SnO2, ZrO2/CeO2 and SnO2/CeO2 nanoparticles. Journal of alloys and compounds, 2012. **513**: p. 359-364.
101. Karunakaran, C., R. Dhanalakshmi, and P. Gomathisankar, Phenol-photodegradation on ZrO2. Enhancement by semiconductors. Spectrochimica Acta Part A: Molecular and Biomolecular Spectroscopy, 2012. **92**: p. 201-206.
102. Selvam, N.C.S., et al., Comparative investigation of zirconium oxide (ZrO2) nano and microstructures for structural, optical and photocatalytic properties. Journal of colloid and interface science, 2013. **389**(1): p. 91-98.
103. Vignesh, K., et al., Photoreduction of Cr (VI) in water using Bi2O3–ZrO2 nanocomposite under visible light irradiation. Materials Science and Engineering: B, 2013. **178**(2): p. 149-157.
104. Sreethawong, T., S. Ngamsinlapasathian, and S. Yoshikawa, Synthesis of crystalline mesoporous-assembled ZrO2 nanoparticles via a facile surfactant-aided sol–gel process and their photocatalytic dye degradation activity. Chemical engineering journal, 2013. **228**: p. 256-262.
105. Agorku, E., et al., Enhanced visible-light photocatalytic activity of multi-elements-doped ZrO2 for degradation of indigo carmine. Journal of Rare Earths, 2015. **33**(5): p. 498-506.
106. Basahel, S.N., et al., Influence of crystal structure of nanosized ZrO 2 on photocatalytic degradation of methyl orange. Nanoscale research letters, 2015. **10**(1): p. 73.
107. Mohan, S., et al., Synthesis and characterization of rGO/ZrO 2 nanocomposite for enhanced removal of fluoride from water: kinetics, isotherm, and thermodynamic modeling and its adsorption mechanism. RSC advances, 2016. **6**(90): p. 87523-87538.
108. Gupta, P.K., et al., Amino acid functionalized ZrO 2 nanoparticles decorated reduced graphene oxide based immunosensor. Journal of Materials Chemistry B, 2017. **5**(10): p. 2019-2033.
109. Pradhan, S., J. Saha, and B. Mishra, Morphology controlled phosphate grafted SnO 2–ZrO 2 nanocomposite oxides prepared by a urea hydrolysis method as efficient heterogeneous catalysts towards the synthesis of 3-substituted indoles. New Journal of Chemistry, 2017. **41**(14): p. 6616-6629.
110. Bandara, W.L.N., et al., Is nano ZrO 2 a better photocatalyst than nano TiO 2 for degradation of plastics? RSC advances, 2017. **7**(73): p. 46155-46163.
111. Zhang, J., et al., Oxygen vacancy-rich mesoporous ZrO2 with remarkably enhanced visible-light photocatalytic performance. Solar Energy Materials and Solar Cells, 2018. **182**: p. 113-120.

112. Reddy, C.V., et al., Synthesis and characterization of pure tetragonal ZrO2 nanoparticles with enhanced photocatalytic activity. Ceramics International, 2018. **44**(6): p. 6940-6948.
113. Kurniawan, R., et al., Synthesis of Iron-Doped Zirconium Titanate as a Potential Visible-Light Responsive Photocatalyst. Indonesian Journal of Chemistry, 2019. **19**(2): p. 454-460.
114. Sampurnam, S., et al., Synthesis and characterization of Keggin-type polyoxometalate/zirconia nanocomposites—Comparison of its photocatalytic activity towards various organic pollutants. Journal of Photochemistry and Photobiology A: Chemistry, 2019. **370**: p. 26-40.
115. Kristianto, Y. and R. Saleh. Effect of CeO2 promotion on the sonocatalytic performance of ZrO2 nanoparticle catalysts. in AIP Conference Proceedings. 2018. AIP Publishing LLC.
116. López, U., et al., Synthesis and characterization of ZnO-ZrO2 nanocomposites for photocatalytic degradation and mineralization of phenol. Journal of Nanomaterials, 2019. **2019**.
117. Raj, S., M. Hattori, and M. Ozawa, Ag-doped ZrO2 nanoparticles prepared by hydrothermal method for efficient diesel soot oxidation. Materials Letters, 2019. **234**: p. 205-207.
118. Dhorabe, P.T., D.H. Lataye, and R.S. Ingole, Adsorptive removal of 4-nitrophenol from aqueous solution by activated carbon prepared from waste orange peels. Journal of Hazardous, Toxic, and Radioactive Waste, 2017. **21**(2): p. 04016015.
119. Lu, Z., et al., Facile microwave synthesis of a Z-scheme imprinted ZnFe2O4/Ag/PEDOT with the specific recognition ability towards improving photocatalytic activity and selectivity for tetracycline. Chemical Engineering Journal, 2018. **337**: p. 228-241.
120. López, R. and R. Gómez, Band-gap energy estimation from diffuse reflectance measurements on sol–gel and commercial TiO 2: a comparative study. Journal of sol-gel science and technology, 2012. **61**(1): p. 1-7.
121. Singh, G., et al., ZnO decorated luminescent graphene as a potential gas sensor at room temperature. Carbon, 2012. **50**(2): p. 385-394.
122. Ding, J., et al., Photoluminescence investigation about zinc oxide with graphene oxide & reduced graphene oxide buffer layers. Journal of colloid and interface science, 2014. **416**: p. 289-293.
123. Sakthivel, B., R. Mohan, K. Ravichandran, A. Nithya, K. Jothivenkatachalam, C. Ravidhas &. J Mater Sci: Mater Electron, 2014. **25**: p. 2546-2553.
124. Pant, H.R., et al., ZnO micro-flowers assembled on reduced graphene sheets with high photocatalytic activity for removal of pollutants. Powder technology, 2013. **235**: p. 853-858.

125. Hosseini, S., et al., Effect of Ag doping on structural, optical, and photocatalytic properties of ZnO nanoparticles. Journal of Alloys and Compounds, 2015. **640**: p. 408-415.
126. Lv, T., et al., Enhanced photocatalytic degradation of methylene blue by ZnO-reduced graphene oxide composite synthesized via microwave-assisted reaction. Journal of Alloys and Compounds, 2011. **509**(41): p. 10086-10091.
127. Wang, R., et al., The characteristics and photocatalytic activities of silver doped ZnO nanocrystallites. Applied Surface Science, 2004. **227**(1-4): p. 312-317.
128. Mustafa, S., et al., Sorption of divalent metal ions on CrPO4. Journal of colloid and interface science, 2005. **283**(2): p. 287-293.
129. Regazzoni, A.E., M.A. Blesa, and A.J. Maroto, Interfacial properties of zirconium dioxide and magnetite in water. Journal of Colloid and Interface Science, 1983. **91**(2): p. 560-570.
130. Muhammad, S., et al., Surface charge properties of zirconium dioxide. Iranian Journal of Science and Technology (Sciences), 2012. **36**(4): p. 481-486.
131. Deo, G. and I.E. Wachs, Predicting molecular structures of surface metal oxide species on oxide supports under ambient conditions. The Journal of Physical Chemistry, 1991. **95**(15): p. 5889-5895.
132. Zhu, C., et al., Photocatalytic degradation of AZO dyes by supported TiO2+ UV in aqueous solution. Chemosphere, 2000. **41**(3): p. 303-309.
133. Li, J., et al., The removal of MO molecules from aqueous solution by the combination of ultrasound/adsorption/photocatalysis. Ultrasonics sonochemistry, 2008. **15**(6): p. 949-954.
134. Chen, M. and W. Chu, Efficient degradation of an antibiotic norfloxacin in aqueous solution via a simulated solar-light-mediated Bi2WO6 process. Industrial & engineering chemistry research, 2012. **51**(13): p. 4887-4893.